TOWARDS THE DEVELOPMENT OF A MIR NOPA FOR TIME-DOMAIN PTYCHOGRAPHY

By

Anthonie de Beer

Thesis presented in partial fulfilment of the requirements for the degree of Master of Science in Laser Physics in the Department of Physics at Stellenbosch University

Supervisors: Dr G.W. Bosman
Dr P.H. Neethling

March 2021

DECLARATION

By submitting this thesis electronically, I declare that the entirety of the work contained therein is my own, original work, that I am the sole author thereof (save to the extent explicitly otherwise states), that reproduction and publication thereof by Stellenbosch university will not infringe any third party rights and that I have not previously in its entirety or in part submitted it for obtaining any qualification.

Date: March 2021

ABSTRACT

This thesis discusses a noncollinear optical parametric amplifier as a source of ultrafast mid-infrared light for spectroscopic experiments and aims to provide a consistent method for the generation thereof. The underlining theory and fundamental principles of this device is outlined as well as various experimental considerations. A design for an experimental setup to generate suitable ultrafast mid-infrared light is proposed and preliminary optical devices are implemented. Generation of a 160 nm bandwidth, near-infrared supercontinuum centred at 1067 nm is shown to be inadequate for the generation of mid-infrared pulses. Parasitic second harmonic-, sum frequency and difference frequency generation processes are also shown to impede mid-infrared generation. These restricting experimental phenomena are highlighted and methods to bypass these limits are given. Finally, as a demonstration of usefulness of such a source of infrared pulses, the novel time-domain ptychographic measurement, HIPPY, of a material's response to mid-infrared light is simulated.

UITREKSEL

Hierdie tesis bespreek die gebruik van ‘n nie-kolineêre optiese parametriese versterker as ‘n bron van ultravinnige middelinfrarooi ligpulse en poog om ‘n metode te voor te lê vir die generasie daarvan. The onderliggende teorie en fundamentele beginsels van hierdie optiese toestel word bespreek asook verskeie eksperimentele oorwegings aangaande die ontwerp. ‘n Ontwerp van ‘n optiese toestel vir die generering van ultravinnige middelinfrarooi lig word voorgestel en voorafgaande eksperimentele opstellings is geimplementeer. Die generasie van ‘n supercontinuum pulse by 1067 nm met ‘n bandwydte van 160 fs word getoon om ongepas te wees vir middleinfrarooi pulse generasie. Parasitiese tweede harmoniek-, som frekwensie- en verskil frekwensie generasie prosesse word ook getoon om middelinfrarooi generasie te verhoed. Verskynsels wat hierdie generasie belemmer word uitgelig met voorgestelde metodes om dit te beperk. Laastens, as ‘n demonstrasie van die nut van infrarooi pulse, is ‘n nuwe tyd gebieds tigografiese tegniek, HIPPY, gesimuleer

ACKNOWLEDGEMENTS

I would like to express my sincere gratitude to Gurthwin Bosman and Pieter Neethling for the opportunity to work on this project and their excellent guidance during the past two years. My gratitude extends to the members of the LRI, whose insights into technical and theoretical matters helped to shape the picture of ultrafast optics in my mind. A thanks to Ruan Viljoen for his help in understanding the Matlab code for the ptychographic reconstruction.

I also would like to acknowledge the CSIR for their financial support in funding my studies.

CONTENTS

LIST OF FIGURES

NOMENCLATURE

List of abbreviations:

AGS	Silver Gallium Sulphide.
BBO	Beta Barium Borate.
CPA	Chirped Pulse Amplifier.
DFG	Difference Frequency Generation.
EM	Electromagnetic.
FWHM	Full Width at Half Maximum.
HIPPY	High-resolution Phase-sensitive spectroscopy with Ptychography
LRI	Laser Research Institute.
MIR	Mid-Infrared.
NIR	Near-Infrared.
NOPA	Noncollinear Optical Parametric Amplifier.
OPA	Optical Parametric Amplifier.
PIE	Ptychographic Iterative Engine.
SFG	Sum Frequency Generation.
SH	Second Harmonic.
SHG	Second Harmonic Generation.
SVEA	Slowly Varying Envelope Approximation.
TBWP	Time-Bandwidth Product.
YAG	Yttrium Aluminium Garnet

1 INTRODUCTION

The invention of the first laser by Maiman in 1960 opened the path for almost all modern-day optics [1]. Shortly after, in 1961, the first harmonic generation was demonstrated [2], opening the door to nonlinear optics and in 1965 the first parametric oscillation was demonstrated [3]. This optical phenomenon has since been extensively studied and used to generate wavelength tuneable light. Parametric oscillation describes a second order nonlinear process, referred to by different names depending on the exact experimental setup. It is a process in which light at a higher frequency (pump) is converted into light at two lower frequencies by the nonlinearity of a medium or vice versa. The parametric nature of the process requires that the lower frequencies add up to the higher frequency in an energy conserving manner. In a setup where parametric oscillation is used to create light at a new wavelength (idler), it is called difference frequency generation (DFG). If parametric oscillation is used to amplify seed light (signal), it is generally referred to as parametric amplification. An optical device that facilitates this process to amplify seeding light or generate new light is called an optical parametric amplifier (OPA) or a noncollinear optical parametric amplifier (NOPA). Noncollinear geometries of an OPA offer shorter pulse durations [4] down to ultrafast pulse durations. Ultrafast pulses are typically the result of the mode locking of many monochromatic waves of light [5]. These waves have a fixed phase relationship and frequency separation between waves, leading to the constructive superposition of the waves and the creation of a short optical pulse. These pulses can have duration down to the femtosecond scale and peak intensities on the order of gigawatts. One application of OPAs and NOPAs is to generate wavelength tuneable ultrafast laser pulses for the spectroscopic investigation of molecular processes, structures, and dynamics [6,7]. These ideas are expanded on and the theory discussed in later sections.

Many molecular processes occur on timescales much shorter than electronic detectors can resolve. This typically occurs at the pico- and femtosecond timescales [8]. These processes include molecular charge transfer dynamics and the excitation of molecular vibrational modes [9,10]. Ultrafast optical pulses of femtosecond duration grant the ability to resolve these fast molecular phenomena by employing stroboscopic pump-probe spectroscopy [11,12]. Ultrafast pulses also lend themselves to nonlinear optics as their short pulse lengths translate into high peak intensities that are ideal for efficient nonlinear optical processes. These spectroscopic experiments require ultrafast pulses with a bandwidth spanning the molecular transition to be investigated. For the investigation of the molecular vibration of organic molecules, we find that most vibrational modes occur in the infrared (0.75-20 μm) [13]. For instance, the carbon-hydrogen (C-H) vibrational stretching mode typically occurs around 3.3 μm. Pump-probe experiments interrogating photo induced isomerisation and charge transfer processes have been performed in the Laser Research Institute (LRI) Ultrafast lab numerous

times at visible wavelengths [14–20]. To extend the spectroscopic capabilities of the lab a mid-infrared source of pulsed light is required. The generation of ultrafast pulses at these wavelengths, however, is not trivial.

The most common source of ultrashort laser pulses is that of a Ti:Sapphire laser, the typical centre wavelength of which is near 800 nm. These pulses are routinely used for DFG or parametric amplification in BBO crystals (BaB_2O_4) and can generate near-infrared (NIR) pulses. These pulses are generally limited to the NIR by the transparency of the crystal. To generate mid-infrared (MIR) pulses in the range 3-10 μm, a different medium that possesses suitable transparency and nonlinear optical properties is required. $AgGaS_2$ (AGS) is one such medium. This birefringent crystal is transparent to a wide range of wavelengths up to 12 μm and has been used to generate ultrashort MIR pulses by DFG of two NIR pulses [21]. Typically, this is done in two stages. First a NIR signal and idler is amplified by parametric amplification in BBO. These pulses then act as the pump and signal in the DFG process in AGS from which the MIR pulses are created.

The aim of this work is to design a scheme for the generation of ultrafast optical pulses in the mid-infrared and provide the necessary methods and tools needed in a consistent manner. This will encompass of all the steps needed to generate tuneable light in the MIR. The design involves the use of the fundamental Ti:Sapphire laser to drive two constructed visible-NIR NOPA's to generate appropriate tuneable NIR pulses, which can finally be used in the MIR-NOPA for MIR generation. A method for the temporal characterisation of MIR pulses is also proposed and its operation is demonstrated. Initial experiments relating to the generation of NIR pulses will be presented. This is the first step in generating MIR pulses. Final experiments with respect to the MIR could not be completed due to infrastructure problems that occurred in the laboratory. Important experimental considerations will also be pointed out and discussed. Lastly, a new and novel ultrafast MIR ptychographic technique, called high-resolution phase-sensitive spectroscopy with ptychography (HIPPY), will be simulated to show how these pulses can be used to investigate material properties.

This thesis is arranged as follows:

- Chapter 2 treats the theory that forms the basis of DFG in a nonlinear crystal as well as autocorrelation as temporal characterization method and the fundamentals of time-domain ptychography.
- Chapter 3 describes the proposed design of the experimental setup for generation of MIR pulses and discusses the important optical elements at each step. It also outlines a ptychographic measurement and how a numeric simulation attempts to reproduce that.

- Chapter 4 presents and discusses a few phenomena to be considered in the design of a MIR NOPA as well as the results of the simulated ptychographic experiment.
- Chapter 5 concludes and summarises the thesis.

2 THEORY

2.1 INTRODUCTION

In order to understand the workings of an infrared NOPA, a few core concepts need to be discussed first. The following theoretical discussion of these various aspects of the propagation and interaction of laser pulses motivate and explain the different elements of the optical setup. These standard theoretical descriptions and derivations are more comprehensively described in [22–24] and this section only aims to describe those concepts that are directly relevant to this study.

2.2 THE WAVE EQUATION

Light, and indeed laser light, is an electromagnetic wave with a time varying electric and magnetic field. As such, it, and its interactions with matter, is governed by Maxwell's equations for electromagnetic phenomena [25]:

$$\nabla \cdot \mathbf{D} = \rho \,, \tag{1}$$

$$\nabla \cdot \mathbf{B} = 0 \,, \tag{2}$$

$$\nabla \times \mathbf{E} = -\frac{\partial \mathbf{B}}{\partial t} \,, \tag{3}$$

$$\nabla \times \mathbf{H} = \mathbf{J} + \frac{\partial \mathbf{D}}{\partial t} \,. \tag{4}$$

From these equations that form the basis of electromagnetic (EM) theory we can derive a wave equation for the propagation of an electromagnetic wave through a nonlinear medium. We assume no free charges, no free currents, and a non-magnetic material. The displacement field, **D**, is related to the electric field by the polarisation. The nonlinearity of the system is contained in the polarisation, **P**, which can be decomposed to consist of a linear term ($\mathbf{P}^{\mathrm{L}}$), and a nonlinear term ($\mathbf{P}^{\mathrm{NL}}$). The displacement field can then be decomposed into the linear displacement field ($\mathbf{D}^{\mathrm{L}}$) and the nonlinear polarization as follows:

$$\mathbf{D} = \epsilon_0 \mathbf{E} + \mathbf{P} \,, \tag{5}$$

$$\mathbf{D} = \epsilon_0 \mathbf{E} + \mathbf{P}^{\mathrm{L}} + \mathbf{P}^{\mathrm{NL}} \,,$$

$$\mathbf{D}^{\mathrm{L}} = \epsilon_0 \mathbf{E} + \mathbf{P}^{\mathrm{L}} \,,$$

$$\mathbf{D} = \mathbf{D}^{\boldsymbol{L}} + \mathbf{P}^{\mathrm{NL}} \,.$$

We see that these assumptions along with the definition of the displacement field lead to the general Maxwell's wave equation for nonlinear optics:

$$\nabla^2\mathbf{E} - \frac{1}{\epsilon_0 c^2}\frac{\partial^2\mathbf{D}}{\partial t^2} = 0, \tag{6}$$

$$\nabla^2\mathbf{E} - \frac{1}{\epsilon_0 c^2}\frac{\partial^2\mathbf{D}^{\mathrm{L}}}{\partial t^2} = \frac{1}{\epsilon_0 c^2}\frac{\partial^2\mathbf{P}^{\mathrm{NL}}}{\partial t^2}.$$

We now define the fields present. With our eye on femtosecond pulses, we define the electric field as a sum of waves at different frequencies. This field is a sum of complex fields, with the real part representing the physical field and summation only over positive frequencies:

$$\mathbf{E}(\vec{\boldsymbol{r}}, t) = \sum_{\mathrm{n}}^{+} \vec{\mathbf{A}}_{\mathrm{n}}(\vec{\boldsymbol{r}}, t)\, e^{i(\vec{\boldsymbol{k}}\cdot\vec{\boldsymbol{r}} - \omega_{\mathrm{n}} t)} e^{i\phi(t)} + \text{c.c.}, \tag{7}$$

where ω_n is the angular frequency of the field, $\boldsymbol{k} = \frac{\omega_{\mathrm{n}} n(\omega)}{c}\hat{\boldsymbol{k}}$ is the wavevector in the direction of the Poynting vector and $\vec{\boldsymbol{r}}$ being the spatial coordinate. $\vec{\mathbf{A}}_n$ is the complex field amplitude and is dependent on the frequency of the specific frequency mode ($\vec{\mathbf{A}}_{\mathrm{n}}(\vec{\boldsymbol{r}}, t) = \vec{\mathbf{A}}(\vec{\boldsymbol{r}}, \omega_{\mathrm{n}}, t)$). This amplitude is assumed to be slowly varying in time and space. For ultrafast pulses, the frequencies are evenly spaced such that, $\omega_{\mathrm{n}} - \omega_{\mathrm{n+1}} = m$, for some constant m, and all the fields have a fixed phase, $\phi(t)$. The complex conjugate is indicated by c.c. and is necessary for the field to be real. The complex conjugate also gives an intuitive way of dealing with negative frequencies as these become part of the complex conjugate to the corresponding positive frequency. A typical shape for the amplitude is that of a Gaussian as in Figure 1. Practically, we find for pulsed laser light, only frequencies within a certain range, $\Delta\omega$, around a centre average frequency, ω_0, have significant amplitudes. We call $\Delta\omega$, the bandwidth and ω_0 the centre frequency. This approach is useful in cases where the bandwidth is much smaller than the centre frequency:

$$\frac{\Delta\omega}{\omega_0} \ll 1\,. \tag{8}$$

For our experiment this holds true for all pulses. As an example, the centre wavelength of our fundamental pulse is 775 nm and has a 6nm bandwidth (FWHM), which gives $\frac{\Delta\omega}{\omega_0}$ three orders of magnitude smaller than 1.

$\phi(t)$ is a time dependent phase term that describes how the frequency changes throughout the duration of the pulse (chirp). The chirp originates as a broadband pulse travels through a medium with a frequency dependent refractive index (dispersive medium). This causes different frequencies to travel at varying speeds in the medium and become spread out in time. For pulses, this manifests as a lengthening of the pulse duration with lower (higher) frequencies shifted to the front (back) of the pulse. This lengthening of a pulse duration can be accounted for via compressor elements in an optical setup. We will assume the chirp to be zero for further discussions.

The FWHM of the temporal intensity ($|\mathbf{E}(\vec{r},t)|^2$), defines the pulse duration, $\Delta\tau$. There exists a minimum pulse duration-bandwidth product for any pulse shape:

$$\Delta\omega\Delta\tau = 2\pi c_B. \tag{9}$$

This means that unchirped pulses with a broader bandwidth will have a shorter temporal profile. The pulse is then called "Fourier" or "transform" limited. This relationship is referred to as the time-bandwidth product (TBWP). The constant, c_B, is dependent on the pulse shape.

When a laser pulse is much longer than a couple of optical cycles of its carrier frequency, the field amplitude can be considered to vary much slower than the oscillation period of the field. This is called the slowly varying envelope approximation (SVEA) in equation (10). What this physically means is that the envelope of the wave must change much slower than the harmonic terms (exponential terms) involving the carrying/average/centre frequency (ω_0) of the wave in both time and space i.e., the change in amplitude is negligible over a propagation distance on the order of the centre wavelength (see Figure 1).

$$\left|\frac{d^2A}{dz^2}\right| \ll \left|k_0\frac{dA}{dz}\right| \qquad \& \qquad \left|\frac{d^2A}{dt^2}\right| \ll \left|\omega_0\frac{dA}{dt}\right| \tag{10}$$

Here the propagation direction is taken to be the z direction and we have the wavenumber of the centre frequency, $k_0 = \frac{\omega_0}{c}$. The effect of this approximation is reducing the wave equation (equation (6)) to only first-order in the spatial coordinate. A similar simplification, the slowly evolving wave approximation [26], can also be used under the additional assumption of a flat phase over the distance of a wavelength. Treating the interaction of light and matter with the SVEA approximation is advantageous as only the temporal evolution of the pulse amplitude need be considered without fast oscillations of the electric field. This simplification becomes apparent in the next section where it will lead to the coupled wave equations.

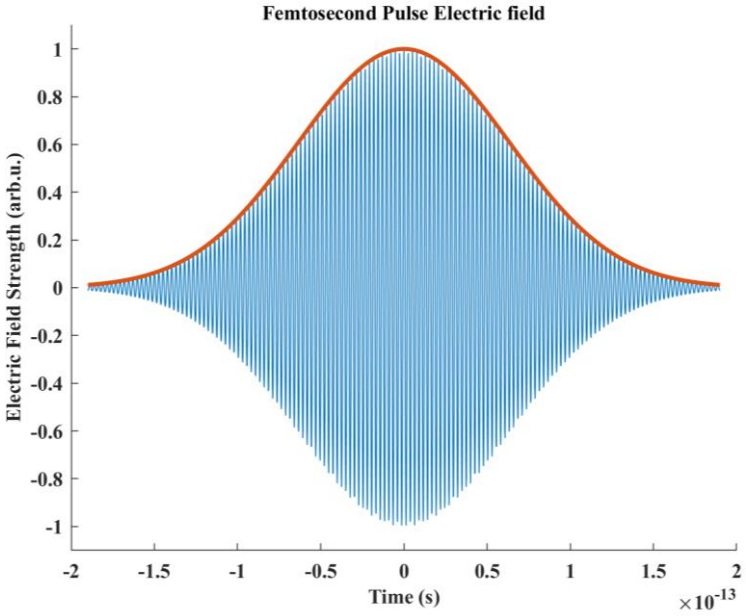

Figure 1: The electric field of a 150 fs laser pulse at 775 nm with a gaussian envelope in time. The field oscillates much quicker than the envelope. In the frame of a single oscillation, the envelope amplitude is approximately constant.

2.3 Polarization, Nonlinear Susceptibility and the Lorentz Oscillator Model

The polarization of a medium is defined as the dipole moment per unit volume. If we consider the dipoles in the medium as electron-nucleus pairs, we can write the polarization of the medium as:

$$P(r,t) = -Nex, \tag{11}$$

where N is the number of dipoles per volume, e is the elementary electron charge and x is the distance between the nucleus and electron.

An incident EM wave interacts with the elementary charges in the medium and induces an oscillating polarisation field in the medium. This polarization field is related to the incident electric field by:

$$\mathbf{P}(\vec{\boldsymbol{r}},t) = \epsilon_0 \chi \mathbf{E}(\vec{\boldsymbol{r}},t), \tag{12}$$

Here χ is the electric susceptibility, a constant of proportionality that relates these two fields, and describes the way in which the medium responds to the incident radiation. Equation (12) holds true when the material response is linear. This is however not true in general. An expansion in the electric field yields an equation for the polarization that contains the higher order nonlinear electric field relation. These terms in turn are coupled to the polarization via higher order susceptibilities. The higher order susceptibilities are tensors, where the tensor indices relate the different polarization

components of the electric fields to the induced polarization in the medium. In summary, we have the 1-dimensional case (single polarization vector) and suppressing $\vec{\boldsymbol{r}}$ dependence:

$$P(t) = \epsilon_0\left(\chi^{(1)}E(t) + \chi^{(2)}E^2(t) + \chi^{(3)}E^3(t) + \cdots\right) \tag{13}$$

$$= P^{(1)}(t) + P^{(2)}(t) + P^{(3)}(t) + \cdots \tag{14}$$

In these equations the important quantity that relates the fields are the susceptibilities. These susceptibilities are properties of the media and will differ between different media not only in strength but also in the optical processes that the higher order susceptibilities lead to. We will look at a non-centrosymmetric medium and only consider the second order susceptibility and one polarization dimension.

$$P(r,t) = \epsilon_0\left(\chi^{(1)}E(r,t) + \chi^{(2)}E^2(r,t)\right) \tag{15}$$

$$= P^{(L)}(r,t) + P^{(NL)}(r,t) \tag{16}$$

A second order susceptibility leads to a number of different processes, amongst them difference frequency generation, the process we will exploit to generate mid infrared laser light. To see how this happens we need to first look at the nonlinear susceptibility, $\chi^{(2)}$.

As the susceptibility is an intrinsic property of the medium, a complete description requires a quantum mechanical approach. It is however possible to describe the nonlinearity of the medium accurately enough to illustrate the rise of optical nonlinear effects by means of classical models [27]. The Lorentz oscillator model classically describes the forces on a charged particle (electron) in an EM field by applying Newton's second law to the interaction between a bound electron and a perturbing EM field. (and does a surprisingly good job at it). We begin by setting up a differential equation for the displacement, $x(t)$, of the electron from the nucleus by assuming a harmonic restoring force along with a damping force and an oscillating external electric field. This reduces to the differential equation for a driven, damped harmonic oscillator, equation (17) that would lead to the linear susceptibility. To include the second order susceptibility, we add a quadratic anharmonicity (for non-centrosymmetric media) to the restoring force, equation (18). The respective differential equations are:

$$\ddot{x} + 2\gamma\dot{x} + \omega_0^2 = \frac{-eE(t)}{m}, \tag{17}$$

$$\ddot{x} + 2\gamma\dot{x} + \omega_0^2 + ax^2 = \frac{-eE(t)}{m}. \tag{18}$$

Here, ω_0, is the resonance frequency, γ, is the damping parameter, and, a, is the strength of the anharmonicity.

We consider a system driven by a net electric field containing two frequencies,

$$E(t) = E_1 e^{-i\omega_1 t} + E_2 e^{-i\omega_2 t}, \tag{19}$$

Following classical perturbation theory wherein we expand in the dimensionless λ:

$$x = \lambda x^{(1)} + \lambda^2 x^{(2)} + \lambda^3 x^{(3)}. \tag{20}$$

we arrive at solutions to the first- and second-order expansion in the displacement, $x^{(1)}$ and $x^{(2)}$. The first order solution contains two terms each dependent on the separate frequencies as in equation (19). The second order solution contains terms, not only at the input frequencies, but also at the sum ($\omega_1 + \omega_2$), difference ($\omega_1 - \omega_2$) and second harmonic ($2\omega_1$ & $2\omega_2$) frequencies. The difference frequency component is given in equation (23). This structure of the second order solution is a tensor of all possible sums of input frequencies.

$$x^{(1)}(\omega_i) = \frac{eE_i}{mD(\omega_i)}, \tag{21}$$

$$D(\omega_i) = \omega_0^2 - \omega_i^2 - 2i\omega_i\,, \tag{22}$$

$$x^{(2)}(\omega_i - \omega_j) = \frac{-2ae^2 E_1 E_2^*}{m^2 D(\omega_i - \omega_j) D(\omega_i) D(\omega_j)}, \quad (DFG) \tag{23}$$

$$i = 1, 2\,.$$

We equate the expressions for the polarization in equations (11) and (12) in order to find an expression for the susceptibilities. Substituting in the expansions of the susceptibility and displacement we arrive at expressions for the 1st and 2nd order susceptibilities that relate the incident electric field to the response of the dielectric medium.

$$P(r,t) = \epsilon_0\left(\chi^{(1)}E(t) + \chi^{(2)}E^2(t)\right) = -Nex \tag{24}$$

$$\epsilon_0\chi^{(1)}E(t) + \epsilon_0\chi^{(2)}E^2(t) = -Ne(\lambda x^{(1)} + \lambda^2 x^{(2)}) \tag{25}$$

$$\chi^{(1)}(\omega_i) = \frac{-Ne^2}{\varepsilon m D(\omega_i)} \tag{26}$$

$$\chi^{(2)}(\omega_i - \omega_j) = \frac{2\varepsilon^2 ma}{N^2 e^3}\chi^{(1)}(\omega_i - \omega_j)\chi^{(1)}(\omega_i)\chi^{(1)}(\omega_j), \quad (DFG) \tag{27}$$

The 2nd order polarization can be concisely written to encapsulate all different incident field polarisations and susceptibility components:

$$P_i^{(2)}(\omega_s) = \varepsilon_0 \sum_{j,k} \sum_{(s;\,m,n)} \chi_{ijk}^{(2)}(\omega_s = \omega_m + \omega_n, \omega_m, \omega_n) E_j\,(\omega_m) E_k(\omega_n), \tag{28}$$

where *i* indicates the polarization direction.

2.4 The Reduced Wave Equation

In a dissipative medium with fields given by summations of complex fields, the wave equation in (6) can be reduced to include the linear refractive index, n:

$$\nabla^2 \mathbf{E_n} + \frac{\omega_n^2 \, n^2(\omega_n)}{c^2} \mathbf{E_n} = \frac{-\omega_n^2}{\epsilon_0 c^2} \mathbf{P_n}^{NL} \tag{29}$$

$$n^2(\omega_n) = 1 + \chi^{(1)}(\omega_n) \tag{30}$$

If we now assume a medium with a second order susceptibility and an input electric field at two separate frequencies:

$$E = E_1 + E_2 = E_1 e^{-i\omega_1 t} + E_2 e^{-i\omega_2 t} \tag{31}$$

From equation (28) the nonlinear polarization resulting from this electric field becomes:

$$P^{(2)}(t) = \epsilon_0 \chi^{(2)}([{E_1}^2 e^{-2i\omega_1 t} + {E_2}^2 e^{-2i\omega_2 t} + 2E_1 E_2 e^{-i(\omega_1+\omega_2)t} + 2E_1 {E_2}^* e^{-i(\omega_1-\omega_2)t} + c.c.] + 2(E_1 {E_1}^* + E_2 {E_2}^*)) \tag{32}$$

These five terms are the five second order nonlinear processes that can be generated by a second order susceptibility. They are, in order, second harmonic generation (SHG) or frequency doubling of each input wave (red), sum frequency generation (SFG) (yellow), difference frequency generation (DFG) (blue) and optical rectification (green). These are all competing processes and can all occur simultaneously. The process responsible for the generation of infrared radiation, however, is DFG. We thus limit ourselves to only this one process, but both SHG and SFG have similar coupled equations. These processes are experimentally suppressed by phase matching which will be discussed in section 2.5.

While only the second order susceptibility is considered here, materials can also exhibit a third order susceptibility. This is the source of third order nonlinear processes such as, the intensity dependent refractive index, self-focussing and self-phase modulation, and beam filamentation. For instance, the third order susceptibility is responsible for the generation of a supercontinuum pulse that is used as a seed in our experiments [24].

The susceptibility tensor can be reduced to a scalar that describes the strength of any one of these processes and we use this effective susceptibility, d_{eff}. The wave equation can now be further reduced to something that can be solved. Our interest is in DFG and the relevant equation under the assumption of a linearly polarized wave propagating along the z-axis, becomes:

$$\frac{\partial^2}{\partial z^2}\mathrm{E_n}(z,t) + \frac{\omega_n^2\, n^2(\omega_\mathrm{n})}{c^2}\mathrm{E_n}(z,t) = \frac{-4\omega_n^2 d_{eff}}{\epsilon_0 c^2} E_1(z)E_2^*(z)e^{-i(\omega_1-\omega_2)t} + c.c. \tag{33}$$

To solve this equation, we utilise the slowly varying envelope approximation, wherein we assume $\left|\frac{d^2A_\mathrm{i}}{dz^2}\right| \ll \left|k_i \frac{A_\mathrm{i}}{dz}\right|$, where A_i refers to the amplitude of the field at frequency ω_i with $i = 1, 2, 3$ and $\omega_3 = \omega_1 - \omega_2$. We reduce to a set of 3 coupled equations for the amplitudes of the two input fields, E_1 and E_2, as well as a generated field, E_3, because of the nonlinear polarization. The nonlinear polarization acts as source term in the wave equation, leading to a new field. If we assume a strong pump wave at the higher frequency input wave (the pump wave at ω_1), such that its amplitude can be taken as constant over the interaction length within the crystal, we now have two coupled equations [22].

$$\frac{dA_S}{dz} = \frac{2i\omega_S^2 d_{eff}}{k_S c} A_P A_I^* e^{(i\Delta kz)} \tag{34}$$

$$\frac{dA_I}{dz} = \frac{2i\omega_I^2 d_{eff}}{k_I c} A_P A_S^* e^{(i\Delta kz)} \tag{35}$$

Here we now have moved to denoting the different electric fields by their role and frequency. The highest frequency input wave at ω_1 is called the pump and is denoted by *P*. The second input wave at ω_2 is called the signal and is denoted by a subscript *S*. The generated wave at ω_3 is called the idler wave and is denoted by *I*. Conventionally, the signal wave has a higher frequency than the idler wave ($\omega_2 > \omega_3$). The wavevector mismatch is also introduced as $\Delta\mathbf{k} = \mathbf{k}_P - \mathbf{k}_S - \mathbf{k}_I$. In the case where $\Delta k = 0$, we have the following solutions to these amplitudes,

$$A_S(z) = A_S(0)cosh(\kappa z)\,, \tag{36}$$

$$A_I(z) = \mathrm{i}\left(\frac{n_S\omega_I}{n_I\omega_S}\right)^{\frac{1}{2}} \frac{A_P}{|A_P|} A_S^*(0)\sinh\left(\frac{2d_{eff}\,\omega_S\omega_I}{c^2\sqrt{k_S k_I}}|A_P|\mathrm{z}\right). \tag{37}$$

As seen in Figure 2, both the signal and idler are amplified as they propagate through the medium. Difference frequency generation is sometimes called parametric amplification because of this amplification of both idler and signal waves.

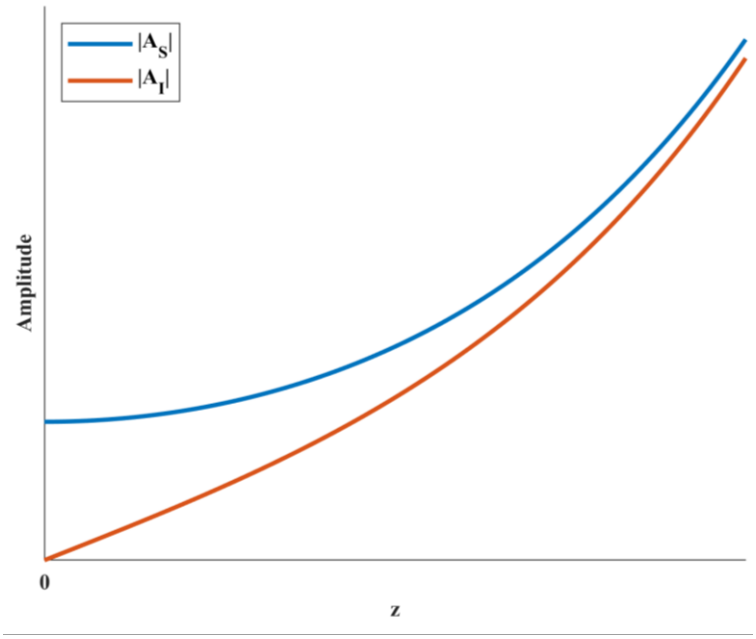

Figure 2: In the case of perfect phase matching, $\Delta k = 0$, we see that both signal and idler wave amplitudes grow exponentially. A detuning from the phase matched case will result in oscillatory behaviour, where the energy oscillates between the signal, idler and pump waves, and prevents any substantial amplification or generation. The signal seeds the process and thus starts with a non-zero initial amplitude, whereas the idler is generated from nothing.

It can be intuitive to think of DFG and parametric amplification by considering the energy level diagram in Figure 3. The diagram illustrates how a pump photon excites the medium oscillator to an excited virtual state. A signal photon at frequency ω_2 can stimulate an oscillator in this virtual state to emit at frequency ω_2. To conserve energy and have a parametric process, an additional photon at the idler frequency, ω_3, must also be emitted. In this way higher energy pump photons are annihilated, while both signal and idler photons are created. This leads to the amplification of the signal and idler.

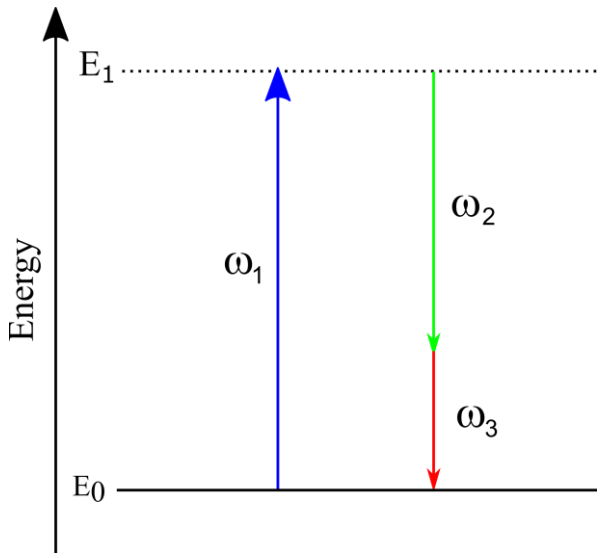

Figure 3: The energy level diagram illustrates DFG. A pump photon with a frequency ω_1, excites (blue) the oscillator from the ground state, E_0, to a virtual excited state, E_1. A signal photon with a frequency ω_2, can stimulate emission (green) of a photon at ω_2 from this virtual state. According to the conservation of energy in this parametric process, another photon at the difference frequency, ω_3, must be emitted (red).

2.5 PHASE MATCHING

As seen in equations (34) & (35), the amplitude, and ultimately the intensity, of the signal and idler waves changes with the wavevector mismatch (Δk). It predicts that the efficiency of the processes is maximised when $\Delta k = 0$. Δk can be considered as a measure of how well energy from the pump is carried over into the signal and idler waves. A large nonzero Δk will result in energy oscillating between waves, as shown in Figure 4.

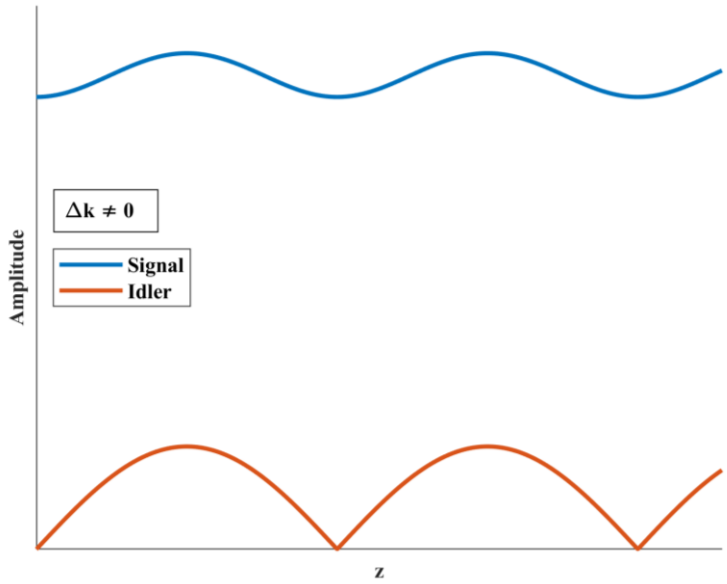

Figure 4: The amplitude of the signal and idler waves oscillates they propagate through the medium when the phase matching condition is not met, $\Delta k \neq 0$.

Figure 5 shows the dependence of the intensity of the generated idler on the wave vector mismatch after propagating a distance L through the amplifying medium. The intensity quickly drops off for increasing values of Δk.

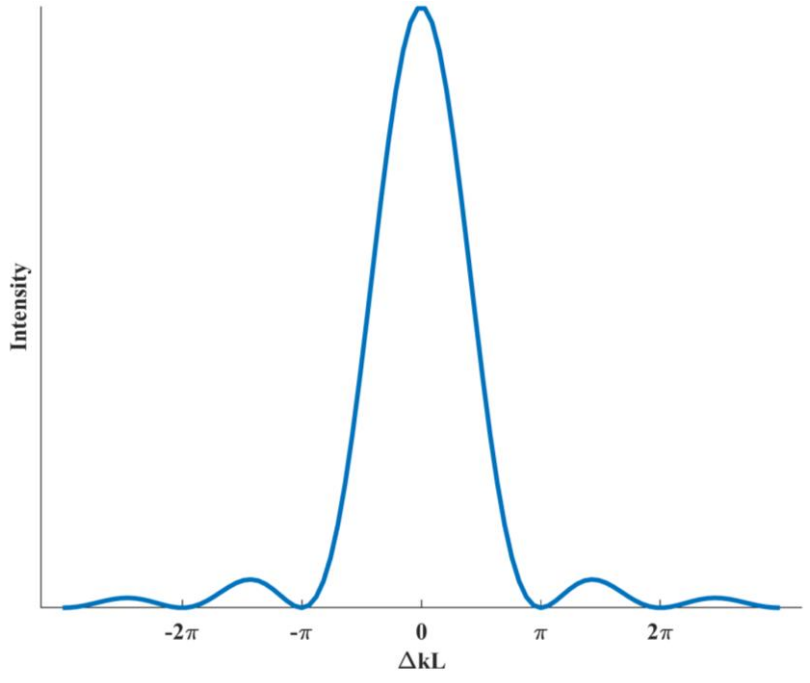

Figure 5: The intensity of the generated idler in a medium of thickness, L, for varying Δk.

We are mainly concerned with the phase matched case, as it generates the strongest idler wave with highest intensity. The process of tuning the wavevector mismatch to zero is called phase matching. To achieve this goal, we consider the wavevector mismatch more closely. If we assume propagation along a common axis, z, the wavevector mismatch can be viewed in terms of the wavenumbers:

$$\Delta \mathrm{k} = \mathrm{k}_P - \mathrm{k}_S - \mathrm{k}_I = \frac{\omega_P n_P}{c} - \frac{\omega_S n_S}{c} - \frac{\omega_I n_I}{c}, \tag{38}$$

$$n_i = n(\omega_i) \quad \& \quad i = P, S, I\,.$$

Setting the wavevector mismatch to zero results in the phase matching condition:

$$\omega_P n_P = \omega_S n_S + \omega_I n_I\,. \tag{39}$$

In general, it is impossible to achieve the matching condition in non-birefringent media because of normal dispersion. Dispersion refers to the changing refractive index, $n_i(\omega)$ for different wavelengths and it generally decreases for longer wavelengths, as in Figure 6, thus making it impossible to satisfy the matching condition. In birefringent media, however, it is possible to find appropriate refractive indices, and thus wavevectors, to fulfil the matching condition by choosing appropriate polarizations for the different fields.

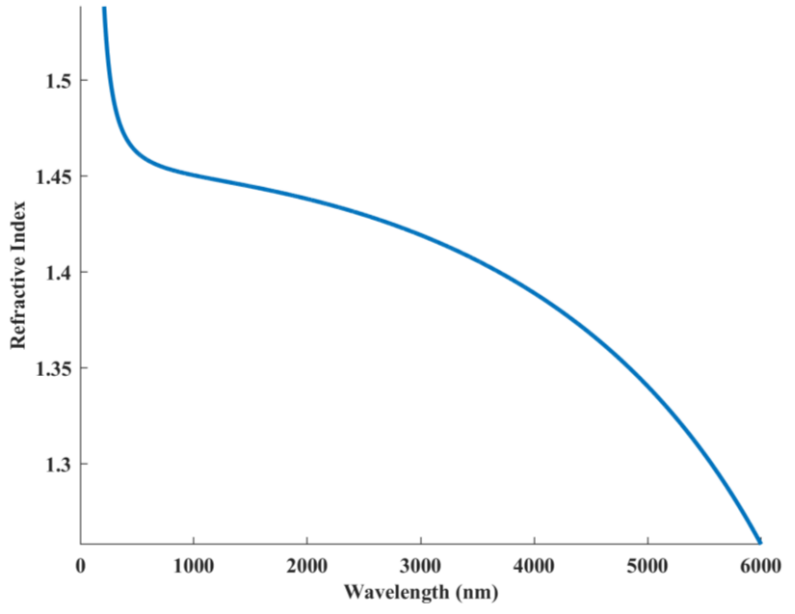

Figure 6: The refractive index for fused silica from the visible to mid infrared wavelengths. The refractive index monotonously decreases for longer wavelengths.

The wavevectors embody the momentum of the light and similarly the wavevector mismatch indicates how well the momentum is conserved. From equation (38) we can see that the mismatch can never be zero for any normally dispersive medium with a monotonously increasing refractive index for increasing frequencies. To circumvent this, a birefringent medium will be used.

2.6 BIREFRINGENCE

A birefringent crystal has two different refractive indices along two different crystal axes. This extra refractive index is a consequence of structural symmetries of the crystal. These symmetries are such that they define an optical axis. Light polarized along this axis will experience a specific refractive index, while light polarised perpendicularly to this axis will experience a different refractive index.

If we think about our Lorentz oscillator model, we can model this as individual oscillators all being able to oscillate in the two different directions with different strengths [5]. If these oscillators are all aligned, the response of the medium to incident light will be dependent on which oscillation is driven i.e., the polarization of the incident light.

Consider an incident electric field with polarization components along $\hat{x}$ and $\hat{y}$, propagating along $\hat{z}$:

$$\mathbf{E}(z,t) = Ae^{i\omega t}\left(\hat{\boldsymbol{x}}e^{ik_x z} + \hat{\boldsymbol{y}}e^{ik_y z}\right) + c.c \tag{40}$$

$$\mathbf{E}(z,t) = Ae^{i\omega t}\left(\hat{\boldsymbol{x}}e^{i\frac{\omega n_x}{c}z} + \hat{\boldsymbol{y}}e^{i\frac{\omega n_y}{c}z}\right) + c.c \tag{41}$$

In the Lorentz model the response of the medium to the driving fields will be different in the two directions. This leads to two different susceptibilities and hence two refractive indices for the different polarizations.

The optical axis is defined by crystal symmetries and wave propagation along this axis has no polarization dependence. Any other propagation direction is polarization dependent and would show birefringence. We distinguish between waves by their polarization with respect to the plane defined by the optical axis and the propagation direction. Waves polarized perpendicular and parallel to this plane are respectively called ‘ordinary’ and ‘extraordinary’.

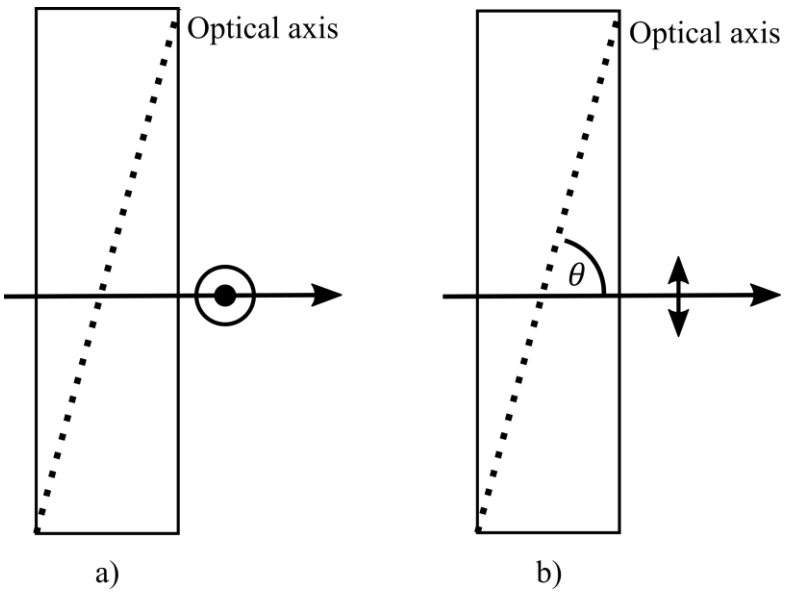

Figure 7: a) Shows the perpendicular polarization of an ordinary wave in a birefringent medium. The ordinary wave has no angle dependence. b) Illustrates the angle dependence of the extraordinary wave. Rotation of the crystal will change θ and change the extraordinary refractive index.

In addition to being distinct from the ordinary refractive index, n_o, the extraordinary refractive index, n_e, also has an angle dependence θ as in Figure 7. For an extraordinarily polarized wave propagating at an angle θ, to the optical axis, the effective refractive index, $n_e(\theta)$, is given by:

$$\frac{1}{n_e(\theta)} = \frac{cos^2(\theta)}{n_o^2} + \frac{sin^2(\theta)}{n_e^2}, \tag{42}$$

where n_e^2 is square of the normal extraordinary refractive index for propagation completely perpendicular to the optical axis. The two refractive indices define two different dispersion relations for different polarizations, as can be seen in Figure 8.

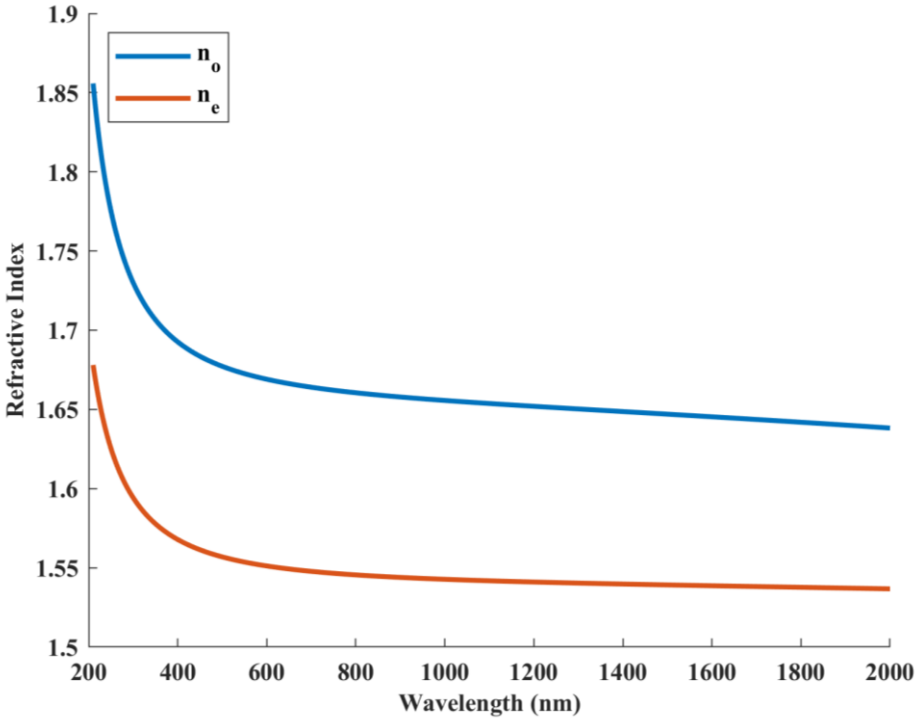

Figure 8: The two refractive indices of a BBO crystal for the visible to near infrared range of wavelengths. BBO is a negative uniaxial crystal, with its extraordinary index being lower than the ordinary index at any wavelength. By angle tuning θ, the extraordinary index can be changed; effectively moving the extraordinary curve up or down.

Generally, there are two different methods to phase match the waves in a uniaxial crystal. These methods, called Type 1 and Type 2, are classified according to the polarizations of the different waves. If the pump wave is polarised (either ordinary or extraordinary) perpendicular to both the signal and idler waves, it is called Type 1 phase matching. These are sometimes written shorthand as *eoo* matching or *oee* matching to quickly indicate the polarizations of the pump, signal, and idler, respectively. If, however, the signal and idler polarizations are perpendicular to each other, it is called Type 2 phase matching. This can be written shorthand as *eoe* or *oeo*.

We will be using Type 1 phase matching with an *eoo* polarization configuration in a negative uniaxial crystal. To do this, we simply substitute the specific phase matching condition into equation (42) and solve for the angle θ. This then sets the angle of the extraordinarily polarized pump with respect to the optical axis.

2.7 Group Velocity

While the phase matching condition can be realised by using a birefringent crystal, the condition is only exactly satisfied for monochromatic pump, signal, and idler waves. Femtosecond pulses,

however, are a superposition of waves and possess a bandwidth around the centre frequency. To handle this, we expand the wavevector mismatch in the detuning of the signal, $\Delta\lambda_S$:

$$\Delta\boldsymbol{k} = \Delta\mathbf{k_0} + \frac{\partial\Delta\mathbf{k_0}}{\partial\lambda_S}\Delta\lambda_1 + \frac{1}{2}\frac{\partial^2\Delta\mathbf{k_0}}{\partial\lambda_S^2}\Delta\lambda_1^2 + \cdots \tag{43}$$

The phase matching in Section 2.5 precisely handles $\Delta k_0 = 0$. To phase match across the bandwidth of the pulse we also require:

$$\frac{\partial\Delta\mathbf{k_0}}{\partial\lambda_S} = 0. \tag{44}$$

This is called broadband phase matching. We will exploit a noncollinear amplification geometry to achieve this condition. Figure 9 shows the noncollinear geometry of the waves in the crystal. Angles α & Ω define the pump-signal angle and the signal-idler angle. Riedle et al. [4] shows how differentiation of the parallel and perpendicular components of $\Delta\boldsymbol{k}$, leads to:

$$\frac{\partial k_S}{\partial\lambda_S}\cos(\Omega) = -\frac{\partial k_I}{\partial\lambda_S}. \tag{45}$$

In terms of the group velocity, v_g, this can be further simplified. The group velocity defines the speed at which a pulse propagates through the medium and is a result of a frequency varying refractive index and can be defined as:

$$\frac{1}{v_{g,i}} = \frac{n_i}{c} + \frac{\omega_i}{c}\frac{\partial n_i}{\partial\lambda_i}, \qquad i = P, S, I. \tag{46}$$

The condition in equation (45) then becomes:

$$v_{g,I}\cos(\Omega) = v_{g,S}\,. \tag{47}$$

This equation now gives an experimentally realisable condition equivalent to equation (44). It states that the idler group velocity projected onto the signal wavevector must be equal to the signal group velocity. The required angle, Ω, can be calculated for the idler and signal for a given pump-signal angle.

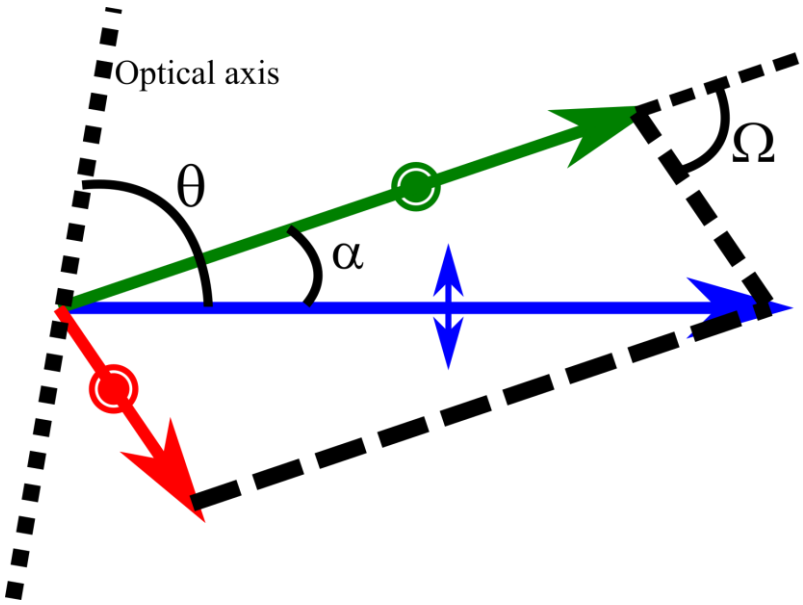

Figure 9: Noncollinear phase matching in a nonlinear crystal with the polarizations and relative directions of the waves. Propagation of the pump (blue) and signal (green) is at an angle of α. Ω is the angle between the signal and idler wavevectors.

2.8 CHARACTERIZATION

In order to characterize an ultrashort optical pulse, we have to reconstruct the electric field in time and determine its spectral content. The transient shape of the pulse typically cannot be measured directly as the timescales involved are much shorter than electronics can resolve. We thus resort to an indirect approach to measuring a pulse in time namely autocorrelation [23].

Optical background free intensity autocorrelation is a technique used to determine the pulse duration of an ultrashort input pulse by overlapping the pulse of interest ($I(t)$) with a variably delayed copy of itself ($I(t-\tau)$) in a nonlinear medium. This overlapping then induces a polarization in the medium which leads to the generation of a new pulse similar to what is discussed in section 2.3, at double the input frequency (SHG). By measuring the autocorrelated intensity ($I_{AC}(t,\tau)$) of this SHG wave for different delays (different temporal overlaps), the duration of the temporal shape of the input pulse can be calculated. Because of the symmetry of the autocorrelation process this calculation requires some assumptions as to the shape of the input pulse.

The intensity of a pulse is proportional to the square of the electric field amplitude:

$$I(t) \propto A^2(t). \tag{48}$$

Following a similar derivation as in section 0 for SHG will show that the field amplitude of the generated second harmonic wave is proportional to the square of the input field amplitude (similar to

equation (37)). By the Poynting theorem, this results in the second harmonic intensity being proportional to the square of the input intensity,

$$I_{SHG}(t) \propto I^2(t). \tag{49}$$

If now we introduce a delay parameter, τ, to one of the input waves and integrate over time, we arrive at exactly the autocorrelation signal that can be measured:

$$S(\tau) = \int_{-\infty}^{\infty} I(t)I(t-\tau)dt\,. \tag{50}$$

The autocorrelation function is a symmetric function. The consequence of this is that no definite pulse shape is determined. However, if an input shape can be assumed e.g., a gaussian, the corresponding pulse duration can be determined via the known ratios of the widths of the pulse and its autocorrelation. For an assumed Gaussian pulse, the corresponding autocorrelation pulse FWHM is:

$$\Delta\tau_{AC} = \sqrt{2}\tau_P\,, \tag{51}$$

where, $\Delta\tau_{AC}$, is the FWHM of the autocorrelation and τ_P is the FWHM of the gaussian pulse.

The ratios of the autocorrelation width to the pulse width for different standard pulse shapes (Gaussian, sech^2, etc) can be explicitly calculated by substitution of a pulse shape in equation (50).

2.9 PTYCHOGRAPHY

Ptychography is a lensless imaging technique that can be used to measure the amplitude and phase of an object field [28]. The general technique is to illuminate a portion of an object and measure the far-field diffraction pattern. The object is shifted so a different portion is illuminated, while sharing some overlap with the previous illumination. This produces a new diffraction pattern that contains some of the information of the previous measurement. This process is repeated until the whole object is scanned. An algorithm is then used to reconstruct the object in amplitude and phase from the recorded diffraction patterns. The ptychographic technique is based on the following relation:

$$I(X,Y) = |\mathcal{F}\{O(x,y)P(x-x1,y-y1)\}|^2, \tag{52}$$

where $I(X,Y)$ is the intensity of the far-field diffraction pattern at the detection plane a distance from the object plane. $O(x,y)$ is the object and $P(x-x1,y-y1)$ is the probe illuminating the object at $(x1,y1)$. $\mathcal{F}$ indicates the Fourier transform.

This idea of reconstructing an object from iterative intensity measurements has been neatly transferred to the time domain where the measured spectrum of a delayed ultrafast pulse overlapped with a temporal object follows a similar relation to equation (52) [29]:

$$I(\omega) = |\mathcal{F}\{O(t)P(t-\tau)\}|^2 . \quad (53)$$

Here, $P(t-\tau)$ is a delayed ultrafast probe pulse. The spectrum, $I(\omega)$, is measured for various temporal overlaps of the probe with the object, $O(t)$. This time domain ptychography picture is in a sense simpler than the original spatial version as it involves only a one-dimensional Fourier transform between the time and frequency domains compared to the two-dimensional transforms needed for imaging. This technique is useful in the time-frequency domain as it can retrieve temporal amplitude and phase modulations imposed on light by interaction with an object.

The same algorithm used in traditional spatial ptychography can be used to reconstruct the temporal object. The Ptychographic Iterative Engine (PIE) is one such algorithm and has been used for time-domain measurements of object functions in the MIR, with a technique called HIPPY [30]. The PIE is given the measured spectra for every delay of the probe as well as the probe shape. Through an iterative process the object function is reconstructed in amplitude and phase. The MIR is sensitive to collective vibrations in a solid. By being able to measure both the amplitude and phase of these oscillations, valuable insight can be gained into the material properties [31]. This is one possible application for the MIR pulses described in this study.

3 Experimental Setup

3.1 Introduction

A suitable laser source for ultrafast spectroscopy requires continuous wavelength tuneability and short pulse durations for the probing of fast molecular processes and transitions. The pulses need also be of high enough intensities to provide sufficient signal strength.

In the visible regime, these requirements are easily met by utilising a noncollinear optical parametric amplifier (NOPA) [32]. A NOPA is an optical system wherein two pulses, a pump, and a signal, are overlapped in a nonlinear crystal. By the process of DFG (also called parametric oscillation) the signal is amplified, and an idler is generated at the difference frequency. We will employ the use of three NOPAs (two visible-NIR and 1 mid infrared) to generate tuneable high intensity mid infrared femtosecond pulses.

A few different approaches to MIR amplification were considered and investigated, including direct amplification from a supercontinuum and the mixing of fs pulses in the visible part of the spectrum from one of the NOPA's with NIR pulses (775 nm) directly from the amplified femtosecond laser. These approaches failed as the efficiencies of both these schemes are very low. Energy considerations drove us to the final 3-phase design which aims to improve on the efficiency of the amplification, giving us higher energy MIR pulses, while also supporting a large tuning range. The final design

requires the mixing of two NIR pulses in an AGS crystal, that has been found to generate MIR pulses efficiently [33,34].

The first, naïve approach was to generate MIR from the DFG interaction between the 775 nm fundamental laser and a visible pulse. This combination of wavelengths proved to be hard to phase match. Another problem was that the shorter wavelength visible pump pulse would not have been of the highest intensity as was the case of a setup pumped by the fundamental 775 nm pulse. From here the possibility of amplifying an NIR signal and MIR idler from a continuum pulse was investigated. Supercontinua in Sapphire and YAG crystals were considered, and it was found that the supercontinuum from of a YAG crystal contains NIR frequencies that could be phase matched. Stable generation of this NIR seed was however a problem along with strong two-photon absorption from the high intensity pump pulse in AGS. All these findings led to and motivated the final design. The general approach of how these first attempts at MIR generation as well as the final design is given in Figure 10.

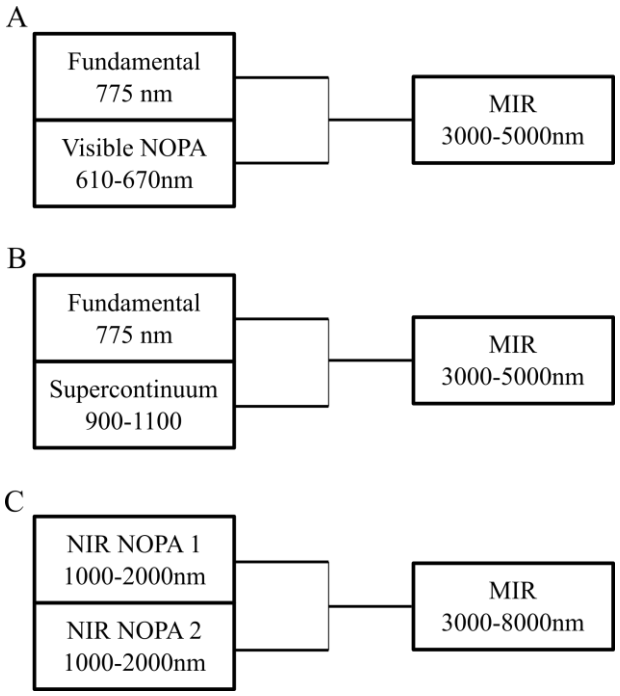

Figure 10: Block diagrams depicting the approaches of initial attempts (A & B) at MIR generation as well as for the final design (C). Diagrams indicate the origin and centre wavelengths of the pulses combined in a nonlinear crystal to generate MIR pulses.

This design required the steering of various wavelengths of light. To do this efficiently, without substantial losses or aberrations, the optics involved need to be suitable for the light incident on them. For the steering of the fundamental 775 nm laser, dielectric mirrors are used. Visible beams and white light continua are steered by aluminium mirrors. Light in the NIR and MIR ranges are steered by silver and gold mirrors, respectively.

3.2 THE PUMP LASER

The energy required for the intensity dependent processes in a NOPA comes from a pump pulse. At the Ultrafast lab at the Laser Research Institute at the Stellenbosch University all the experiments on the optical table are driven by a Clarke-MXR CPA-series laser. This laser delivers 775 nm pulses with a pulse duration of 150 fs at a rate of 1 kHz. The typical pulse energy is 700 μJ per pulse. This type of pump pulse is particularly suited to conduct ultrafast pump-probe spectroscopy experiments.

These pulses are split via beam splitters and directed to the optical setups needed for the current experiment, typically a pump and probe preparation stage, after which the beams are directed to the sample and detector group. With a pump-probe experiment in mind, we split the fundamental pulses from the CPA into three beam paths. One to prepare a pulse for sample excitation and two to prepare the infrared probe pulse.

3.3 NIR NOPA

To generate the pulses needed for the difference frequency generation of mid infrared pulses, we require two separate visible-NIR NOPAs. A diagrammatical layout of the visible-NIR NOPAs is given in Figure 11, with the optical elements labelled. Only about 200 μJ of the fundamental pulse energy is used as input for a single visible-NIR NOPA. In this NOPA, a portion of the high intensity near infrared pump pulse drives a supercontinuum (“white light”) generation process at (3) in the Figure 10. The remaining fundamental energy is used for SHG in a BBO crystal located at (5). At (7) in the diagram, the white light and a fraction of the second harmonic (SH) pulses are overlapped in another BBO crystal for parametric amplification to amplify a temporal slice of the white light signal. This process is repeated to further amplify the signal at (16).

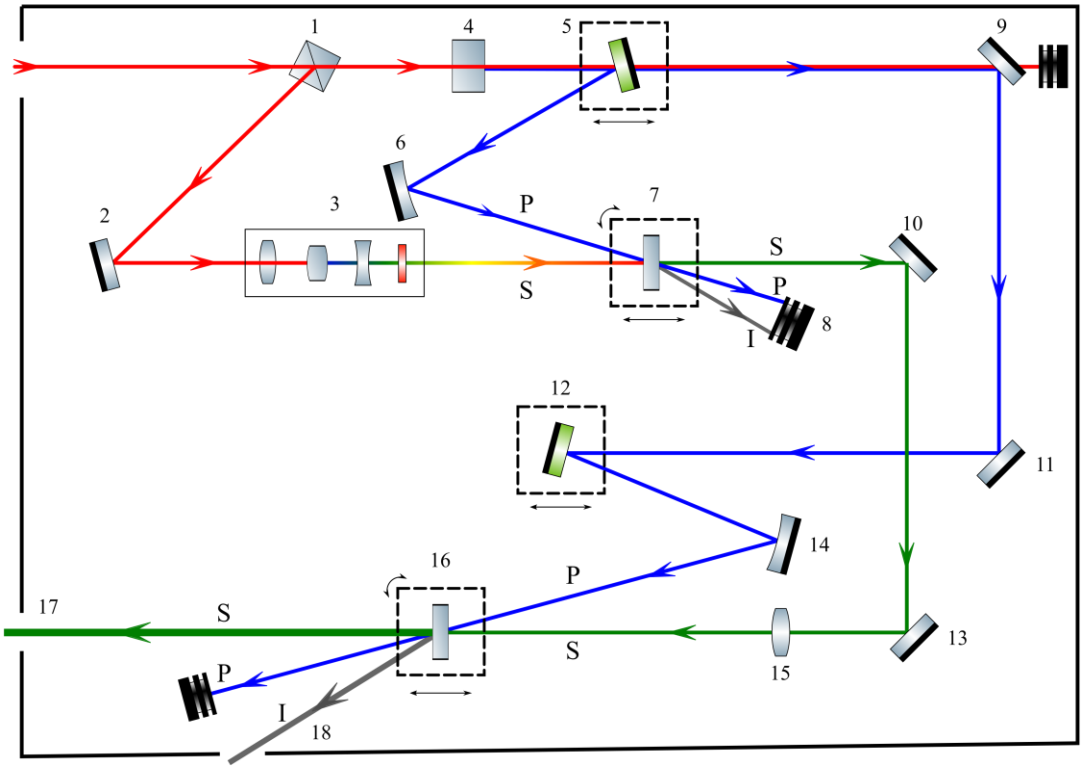

Figure 11: Diagram of the setup of the visible-NIR used to generate tuneable NIR pulses. The fundamental 775 nm pulse enters at top left. The important optical elements are labelled and described in the text below. The generated visible and NIR exit the setup in the bottom left (17 & 18) and are then further directed by the appropriate mirrors.

The following sections will discuss each of the important steps along the beam paths and explain how a NOPA generates a tuneable NIR pulse. References to elements in Figure 11 will be made by the corresponding element number in brackets.

3.3.1 SUPERCONTINUUM ("WHITE LIGHT")

To generate a supercontinuum for seeding the parametric process, 12 mJ of the pump pulse is diverted by a beam splitter (1) and directed by a mirror (2) into the white light generation stage (3). This stage consists of various optical elements. The pulse first passes through a neutral density filter and adjustable iris to fine tune the pulse intensity and numerical aperture. It is then focused into a 3 mm sapphire crystal where the supercontinuum generation takes place. This process occurs at very high intensities and control over the input intensity and aperture is important to generate single filament white light without damaging the crystal [35]. Single filamentation of the white light is important as it has good pulse to pulse power stability. The generated white light continuum is a highly chirped pulse. This means that the pulse duration is much longer than the input 150 fs pulse. The spectral content of the pulse is also temporally dispersed, with longer (red) wavelengths shifted to the front of the pulse and shorter (blue) wavelengths moved to the back of the pulse. This long, chirped pulse is

important for the tunability of the NIR NOPA as we overlap a much shorter pulse with a section of this white light to select a wavelength region for amplification. After the white light is generated, it is recollimated and passed through a lowpass filter to remove the remaining 775 nm light and directed into the amplification crystal (7).

3.3.2 388NM SECOND HARMONIC GENERATION

After passing through the beam splitter at (1) the pump pulse passes through a 0.7 mm BBO crystal (4) where SHG occurs to produce a pulse centred at 387.5 nm. The BBO crystal is cut such that a beam incident perpendicularly, will propagate through the crystal at 30.2° to the optical axis. The crystal is also on an angle adjustable mount. The cut of the crystal and the adjustable mount make for easy tuning of the phase matching angle and efficient SHG. This second harmonic pulse (SH) is used to pump both parametric processes in crystals (7) and (16).

3.3.3 AMPLIFICATION

Amplification and generation of ultrafast broadband pulses in a nonlinear crystal depend on many factors. Firstly, as DFG is an intensity dependent process, higher incident light intensities improve the efficiency of the process. High nonlinearity of the crystal also improves the nonlinear response. The refractive indices of the birefringence affect the bandwidth that can be amplified and the wavelengths that can be mixed. The group velocity dispersion also comes into play, as different pulses propagate at different speeds and thus separate from each other, losing temporal overlap and generating pulses of longer duration. This can be countered by using a thinner crystal to increase the gain bandwidth but at the cost of the amount of amplification. All these factors as well as identifying a crystal that is transparent in the wavelength range of interest and exhibits good thermal and optical properties, must be finely balanced to optimally generate the tuneable pulses.

Pulse amplification occurs first in the BBO crystal at (7) and the second crystal at (16). Approximately 20% of the SH is reflected off a beam splitter (5). This splits the energy of the 388 nm pulse between the first and second amplification stages. This pulse is then directed by a focusing mirror into the crystal at an angle (the noncollinear angle) to the white light beam. The focus is about 10 mm in front of the crystal.

An important aspect to parametric amplification and generation, is the overlap of optical pulses. Not only do the pulses have to overlap spatially with intersecting beams, but they must also be temporally overlapped. This means that they must be in the same spot in the crystal at the same time (two cars can only crash if their routes intersect and they happened to be at that intersection simultaneously). To temporally overlap two pulses originating from a beam splitter, the duration of travel for each

pulse must be equal at the point of intersection. This travel time can be expressed by the speed (c) and the pathlength (x) travelled, $x = ct$. Light travels at a constant speed in air and thus if the pathlengths travelled is equal, the pulses shall overlap temporally at the intersection. Various optics introduce additional pathlength because of their refractive indices that alter the pulse speed. The translation stages at (5) and (12) allow as to adjust the pathlength of the pump pulse to equal that of the signal where they intersect in the crystals (7) and (16) respectively.

The duration of a pulse (Δt) also defines a spatial pulse length, $\Delta x = c\Delta t$. The two pulses are overlapped in the crystal for amplification. Adjustment of the translation stage at the beam splitter (5) is used to change the temporal overlap of the SH with the white light. The supercontinuum pulse is a heavily chirped, broadband pulse, with a much longer duration, and thus length, than the SH. As the SH is much shorter than the white light, it is only ever overlapped with a section of the white light and the wavelengths contained therein. Adjusting the pathlength of the SH, changes this overlapping section and thus the wavelength overlapped with the SH. We thus select the amplified wavelength by adjusting the temporal overlap of the white light continuum with the SH.

Using the mount at (5) and (6) we can adjust the noncollinear angle appropriately according to the group velocity matching condition. The mount of the crystal (7) is used to adjust the phase matching angle made with the SH. The BBO crystal (7) can also be moved closer to the focus for higher intensity. Care must be taken to not move to close to the focus, as this might damage the crystal or reduce the spot size of the SH such that the pulses no longer spatially overlap.

If done correctly, three beams will exit the crystal. The remaining pump as well as an initial NIR idler is dumped at (8). The amplified signal is directed by mirrors (10) and (13) to the second amplification stage. 388 nm SH light is also transmitted at (5) and further directed by mirrors (9), (11), (12) and (14) to the second amplification stage.

This second stage functions similarly to the first, now further amplifying the signal and generating the NIR idler used in the MIR NOPA. The mirror and translation stage at (12) functions like the beam splitter (5), controlling the pump path length and thus spatial overlap of pulses. A focussing mirror (14) again focuses the pump in front of the BBO crystal (16) at an angle to the signal pulse. The signal is slightly focused by a long focal length mirror (15), reducing its spot size. This is done both to increase the intensity and ensure that the pump spot size is greater than that of the signal for maximal nonlinear interaction.

After amplification at the second BBO crystal (16), the visible signal (17) as well as the generated NIR idler (18) is much more intense than after the first stage. These are the output pulses and both

pulses can be extracted from the setup for use in a spectroscopic experiment. In this case, the NIR idler at (18) will be directed to a secondary setup for generation of MIR pulses.

The centre wavelength of the NIR idler is dependent on the chosen signal wavelength by temporal overlap. The visible signal of this setup can be tuned between 480 nm and 600 nm. By assuming a constant pump wavelength at 388 nm, we can calculate the centre idler wavelengths. This is shown in Figure 12.

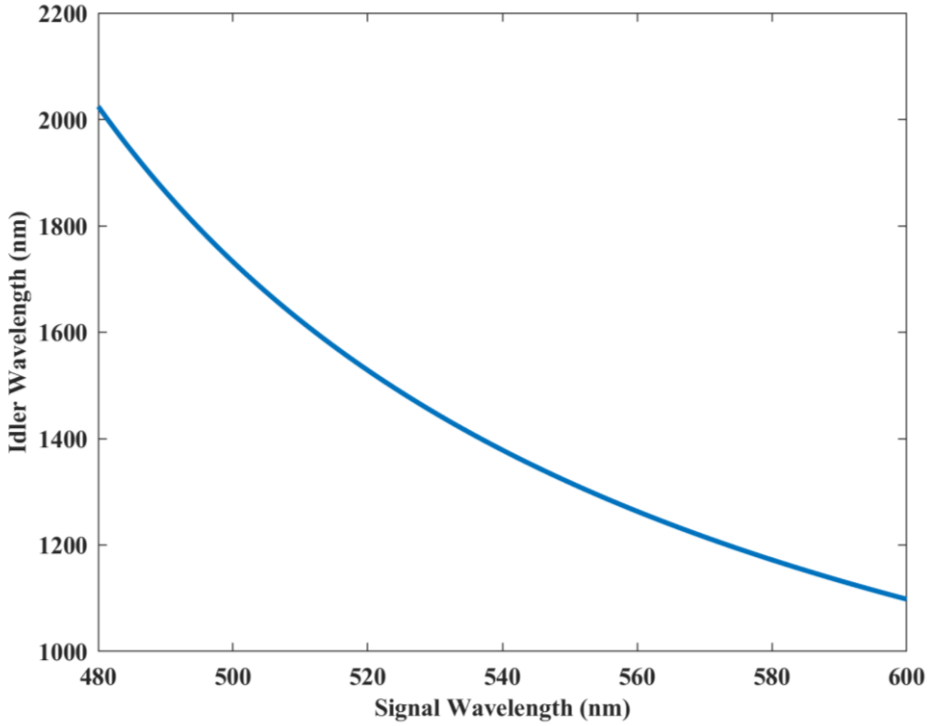

Figure 12: Calculated idler wavelengths for DFG of a signal with a fixed 388 nm pump.

3.4 MIR NOPA

The visible-NIR NOPA satisfies all the requirements of our light source but one: a mid-infrared wavelength range. The tuning range of a visible NOPA is limited by the nonlinear crystal responsible for the parametric process. The existing NOPA uses BBO crystals for the nonlinear processes. This crystal however is not suitable for the generation or amplification of mid-infrared pulses.

The coupled wave equations set out in Section 2, are theoretically valid for any combination of frequencies. The limitation lies in the nonlinear medium, as it is typically only transparent without absorption and with a high nonlinearity for a limited range of frequencies. Phase matching also needs to be considered, as the birefringence of the crystal might not allow phase matching of certain frequencies. Furthermore, nonlinear crystals need to be cut at certain angles to internal symmetries, that are sometimes difficult to realise. The damage threshold of the crystal also needs to be adequate

for high intensity pulses even though a parametric process does not deposit energy in the crystal. BBO-based NOPAs are thus only able to amplify pulses up to about 2.4 μm [36].

To generate and amplify infrared pulses in the range 3-10 μm, we require a different crystal. We turn to silver thiogallate ($AgGaS_2$), henceforth AGS, as a suitable nonlinear crystal in the infrared. This crystal is transparent in the range 0.53-12 μm and phase matchable throughout with NIR pulses, promising a very wide degree of tuneability. The nonlinearity of AGS is 31 pm/v, which is lower than that of other infrared nonlinear crystals such as $ZnGeP_2$ (111pm/V) and GeSe (63 pm/V) (Eksma optics). Despite the lower nonlinearity, AGS has been successfully used to generate mid-infrared femtosecond pulses [21,37,38].

A NOPA pumped by an 800 nm centre wavelength can amplify signal and idler waves both in the NIR region 1.2-2 μm. When these pulses are then used for DFG in AGS, efficient MIR pulse generation occurs [39]. In this experiment similar pulses are used, but they are not products of a single NOPA, but of 2 different NOPAs. This adds a degree of freedom in the choice of signal and idler as they can be set to a wavelength independent of each other.

Another reason for choosing this multi stage setup over the setup of a single NOPA pumped by the 775 nm fundamental pulse, is that AGS displays significant two-photon absorption at wavelengths shorter than 800 nm [40]. Consequently, better efficiencies are found by pumping the parametric process in AGS with pulses deeper in to the infrared (1-2 μm) [39].

The proposed setup is diagrammatically represented in Figure 13. The idlers generated by two separate visible-NIR NOPAs, (1) & (2), now act as the pump and signal, with the shorter wavelength pulse chosen to be (1). Similarly, for amplification in the MIR NOPA, the two pulses are overlapped in the AGS crystal (5) at a noncollinear angle. This angle is determined by the group matching condition for the given signal and expected idler. Temporal overlap is optimised by the delay stage at (3). The remaining pump and idler after amplification are blocked (6) and the generated MIR idler is reflected (7) and directed out of the setup (8). From here it can be directed to an autocorrelator for temporal characterization or an infrared spectrometer to determine spectral content.

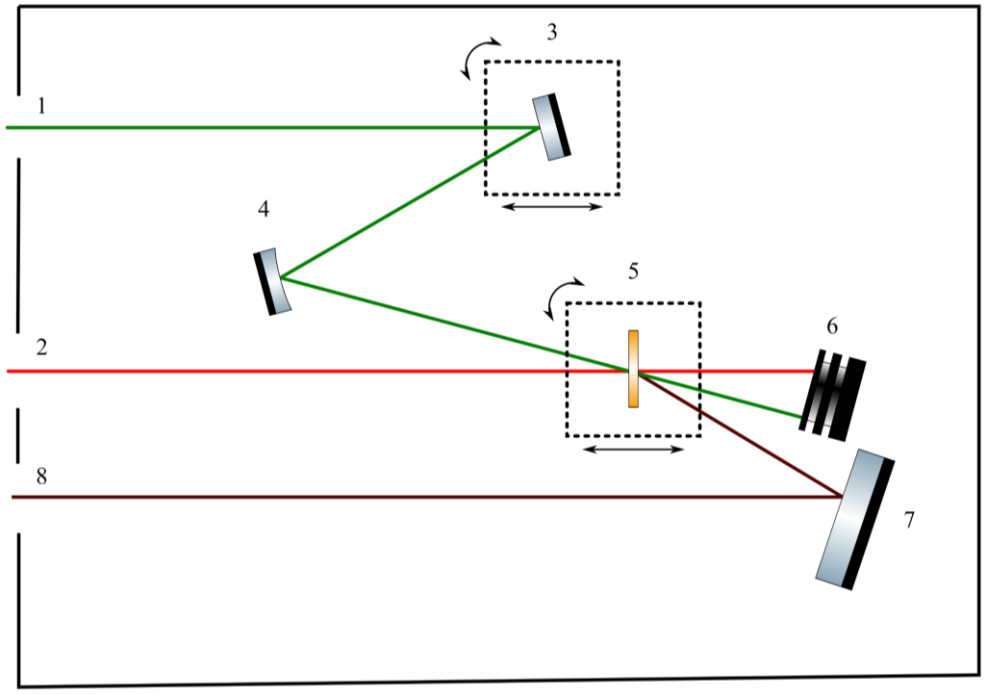

Figure 13: Diagram of the noncollinear generation of mid infrared pulses by mixing 2 NIR pulses (green and red) in an AGS. Incident beams enter the setup from the left (1 & 2) and the MIR beam exits at (8). Optical elements are again numbered.

3.5 AUTOCORRELATOR

As discussed in Section 2.8, temporal characterisation of the generated pulses is done by directing them into a second harmonic autocorrelator. This device uses the nonlinear process to measure pulse duration. The pulse to be measured is mixed with a copy of itself in a nonlinear optical crystal. The crystal used is a 0.4 mm thick AGS crystal, as it is transparent in the regime of the measured pulses (MIR) and in the regime of the second harmonic (NIR). The crystal is cut at 34° to the optical axis.

The autocorrelator design is of a background free nature in that the pulses are overlapped noncollinearly. The background is removed because the only second harmonic signal detected is from the overlap of the two incident beams (the autocorrelation) and no second harmonic generated from a single beam reaches the detector. The layout of the autocorrelator is shown in Figure 14.

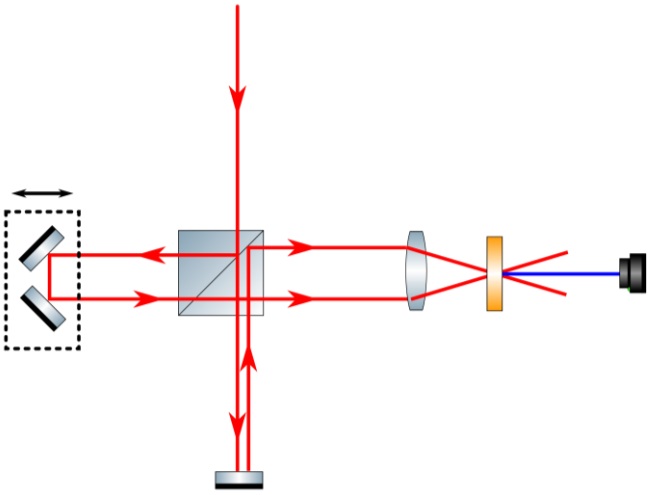

Figure 14: The autocorrelator design for measurement of the pulse duration. Input light is split by a 50/50 beam splitter. One of the split beam's path length is controlled by a translation stage that moves a retroreflector. The beams are focused noncollinearly in the AGS crystal to generate a second harmonic signal dependent on the delay between the pulses. The intensity of the second harmonic is measured for every delay increment.

The overlap of the pulses is changed by a micro-stepping motorised linear translation stage. This translation stage changes the path length travelled by one pulse and changes the delay between the pulses. The intensity measured as a function of time while the motor moves the pulses through temporal overlap. The speed of the stepping motor is set such that the intensity can be averaged at each step. The result is an intensity profile as a function of time while the motor moves. To convert to an axis of delay times, the speed and step size of the translation stage are needed. From this delay axis an autocorrelation FWHM, $\Delta\tau_{AC}$, can be measured for this profile. From $\Delta\tau_{AC}$ the FWHM of the Gaussian input pulses can be determined.

3.6 Time-Domain Ptychography Simulations

Time-domain ptychography is used to reconstruct complex object functions with amplitude and phase from measured intensity spectra, as discussed previously in Section 2.9. This makes it ideal for the spectroscopic investigation of the vibrational modes of a nonlinear material where the response of the material is a time dependent function with a distinct frequency and phase structure in the Fourier transformed frequency space.

This has been done in a sum frequency generation setup [30] that successfully reconstructed an object pulse in time. The sum frequency was generated by mixing a narrowband NIR probe and a broad IR pulse. The IR pulse bandwidth covers the vibrational modes of interest. The interaction of the linear

susceptibility of the medium with this IR pulse creates a linear polarization, $P_L(t)$. The sum frequency field is then related to these input fields by:

$$E_{SFG}(t) \propto E_{NIR}(t-\tau)\, P_L(t). \tag{54}$$

The measured quantity is the spectral intensity, $I(\omega)$, of the SFG at various delay times of the probe. From equation (53) we now have:

$$I(\omega) = |\mathcal{F}\{\, P_L(t) E_{NIR}(t-\tau)\}|^2. \tag{55}$$

Here, the linear polarization is the object pulse to be reconstructed and the NIR field is the known delayed probe.

Simulating a time-domain ptychographic reconstruction involves the generation of the spectra for different temporal overlaps of the linear polarization and delayed probe. These spectra are combined into a spectrogram that is fed into the iterative engine. To generate these spectra the SFG process needs to be simulated by defining a variable delay probe pulse in time as well as the broadband IR pulse and material susceptibility.

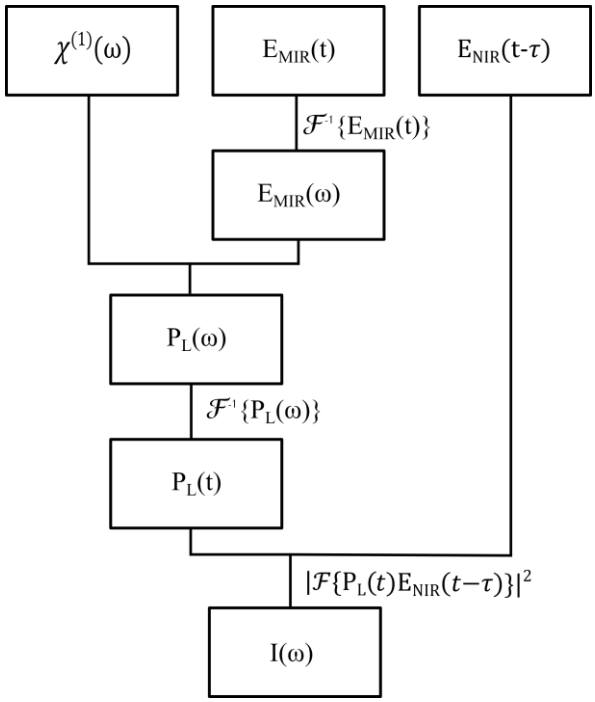

Figure 15: A diagram setting out the procedure for generating a simulated spectrogram, $I(\omega)$, from the defined linear susceptibility, MIR and NIR pulses ($\chi^{(1)}(\omega)$, $E_{MIR}(t)$ and $E_{NIR}(t-\tau)$). Fourier transforms and inverse Fourier transforms are indicated where needed.

The probe is defined in time as a Gaussian pulse centred at 775 nm with a duration of 1.72 ps and no additional phase or chirp. Similarly, the IR pulse defined as a Gaussian pulse centred at 3.3 μm with

a duration of 67 fs. The complex linear susceptibility is defined in frequency as a sum of Lorentzian lines. To create the complex object function the Fourier transformed IR pulse is multiplied with the susceptibility in frequency space and then transformed back to the time domain by an inverse Fourier transform. These are the functions that describe the probe and object pulses. A spectrogram can be retrieved by the absolute value of the Fourier transformed product of the pulses as in equation (55). Figure 15 shows a diagrammatical representation for this process.

We now have our simulated measured data that can be fed into PIE. We expect the algorithm to reconstruct the object pulse and can check this by comparing to the original input. Only the amplitude of the object pulse is investigated in this simulation, but in principle the phase can also be reconstructed with this ptychographic approach.

The code used to perform the ptychographic reconstruction is that used by [30] to recover a real object pulse from measured spectra. The simulated measured data in this experiment is written to match those conditions (wavelengths and vibrational structure) as well as simulate possible pulses generated by the MIR NOPA. The results of these simulations and reconstructions are presented in Section 4.4.

4 Results and Discussion

4.1 Preliminary Supercontinuum

MIR pulses are to be generated by DFG between NIR pulses. Early experiments explored the feasibility of using a supercontinuum generated from a YAG crystal to supply the NIR radiation needed. The conventional approach would then have been used to amplify the NIR wavelengths in the continuum to produce a usable NIR pulse. The centre wavelength of this pulse would also easily be tuned by temporal overlap.

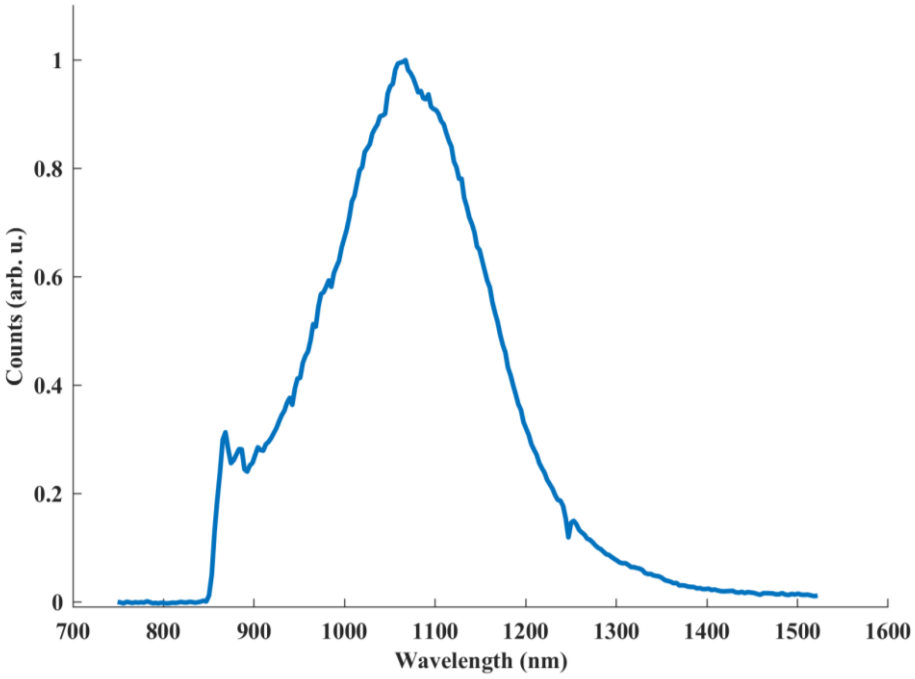

Figure 16: The measured intensity spectrum of the supercontinuum generated in a 2 mm YAG crystal pumped by a 150 fs 775 nm pulse. An 850nm long pass filter was used to block off remaining pump light.

Figure 16 show the measured spectrum. This spectrum is centred at 1067 nm with 160 nm FWHM. This continuum would need to be mixed with the 775 nm fundamental to amplify and generate MIR pulses.

This spectrum grants us access to NIR wavelengths and could conceptually be mixed with another NIR source for DFG of MIR light, but the intensity of the light is too low. Incident NIR pulses act as a seed for the DFG process, and as such, higher intensities would benefit amplification. The 775nm pulse also undergoes significant two-photon absorption in AGS, further reducing amplification. These two factors prevent the generation of MIR pulses from the DFG mixing of continuum NIR and fundamental 775nm pulses.

4.2 AUTOCORRELATION

To verify the rated pulse duration of the Clarke-MXR CPA laser and demonstrate the background free autocorrelation technique, the pulse duration of the fundamental pulse is measured.

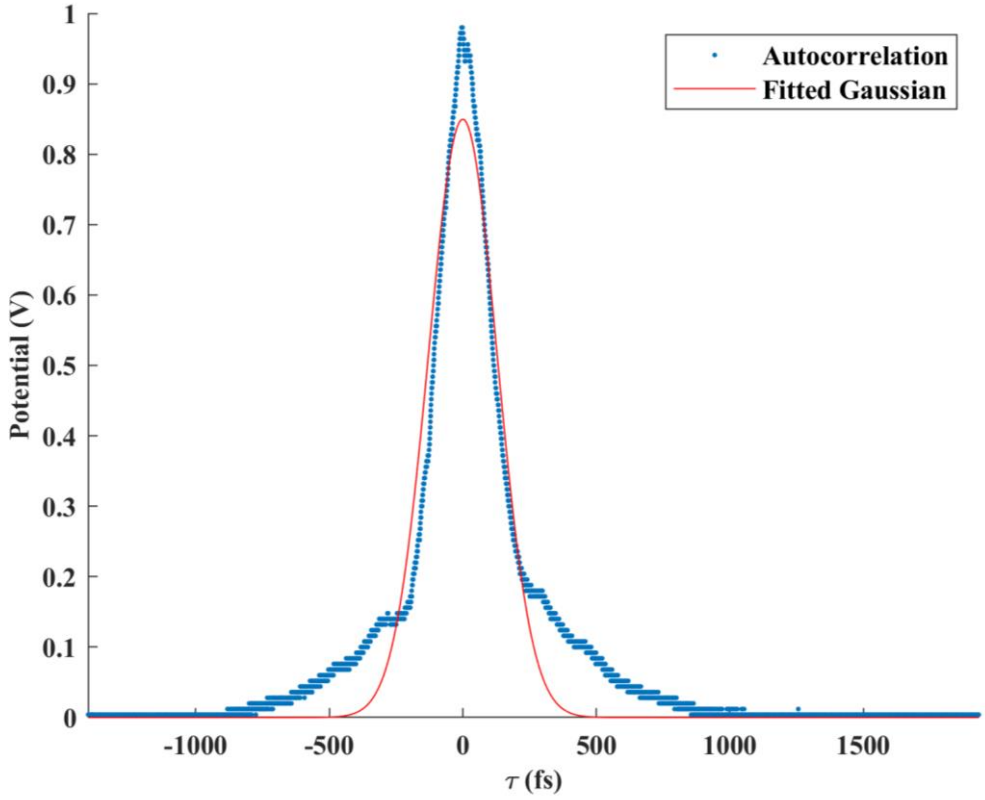

Figure 17: The background free autocorrelation trace of the 775 nm fundamental pulse as a function of the relative delay of the two pulses (τ). A Gaussian pulse fitted to the data has a FWHM of 214 fs.

A Gaussian fit to the autocorrelation has a FWHM duration of 214 fs. The duration of the input pulse is determined to be 151 fs.

4.3 DFG IN BBO AND ACCOMPANYING PARASITIC PROCESSES

The visible-NIR NOPA's supply the NIR pulses to be mixed in AGS for the generation of MIR pulses. As described in Section 3.3, this process involves the mixing of visible pulses in BBO crystals. The second order nonlinearity of BBO, however gives rise to various other processes like sum frequency generation and second harmonic generation as mentioned in Section 2.4. These processes can normally be suppressed by the phase matching condition to ensure the dominance of one process. Despite this suppression, it is still possible for more than one process to occur simultaneously. In a situation where additional nonlinear processes occur and decrease the efficiency of the main sought-after process, they are called parasitic processes.

In an early DFG experiment where a NIR pulse centred at 1200 nm was mixed with the fundamental pulse in a 2 mm thick BBO crystal to produce 2.2 μm pulses by DFG, these parasitic processes showed up in the most spectacular way. Figure 16 is a photo of the beams exiting the crystal on a viewing card. These visible beams are not the expected invisible MIR and NIR light. Measuring the

spectra for each of these beams reveals that there are in fact 4 parasitic processes occurring, some of which are not directly generated by the incident light.

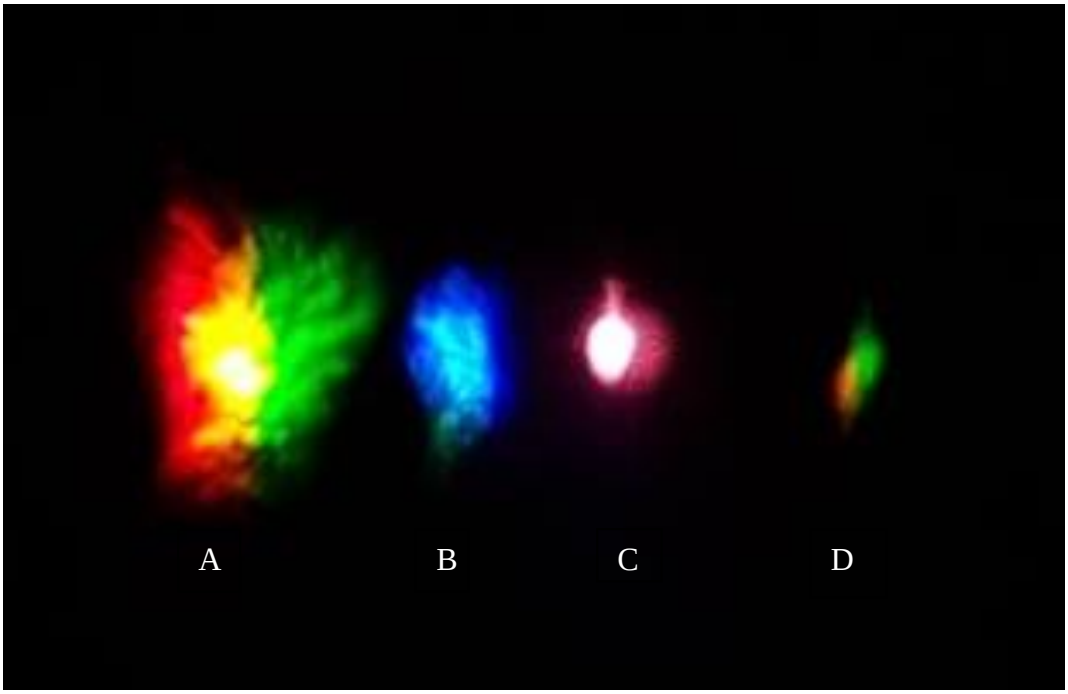

Figure 18: A photo of the pulses exiting a BBO crystal pumped noncollinearly by 775 nm fundamental pulses and a 1200nm NIR signal pulses. On the left (A) we have the second harmonic of the NIR pulse (~600 nm). Centre left (B) is the sum frequency generated by the fundamental and NIR pulses (~480 nm). Centre right (C) shows the remaining fundamental pulse and its second harmonic (388 nm). The fundamental is much more intense and displays brighter on the viewing card. On the right (D) the difference frequency generated by NIR (1200 nm) and SH (388 nm) at about 580 nm.

On the left in Figure 18 we have the second harmonic generated by incident 1200 nm NIR pulse with a wavelength range from about 580 nm to 640 nm (A). This beam exits the crystal collinearly with the remaining NIR radiation. 3rd from the left (C) we have the remaining light from the incident pump at 775 nm. A spectrometer reveals that this beam also contains 388 nm light – the second harmonic of the pump. The blue light is not visible as the much higher intensity pump fluoresces brightly on the viewing card.

From these four incident- and second harmonic beams two more parasitic processes are born. 2nd from the left (B) is a blue pulse generated by the sum frequency of the fundamental pulse and the 1200 nm NIR pulse. This pulse is centred at about 480nm. Its location between the pump and NIR pulses is in accordance with where sum frequency is expected to be generated in a noncollinear amplification setup.

On the right (D) the fourth beam is found to be the difference frequency generated by the incident NIR pulse and the second harmonic of the fundamental pulse. This pulse is centred at 570 nm. This secondary amplification by a pulse generated in the same crystal was not expected.

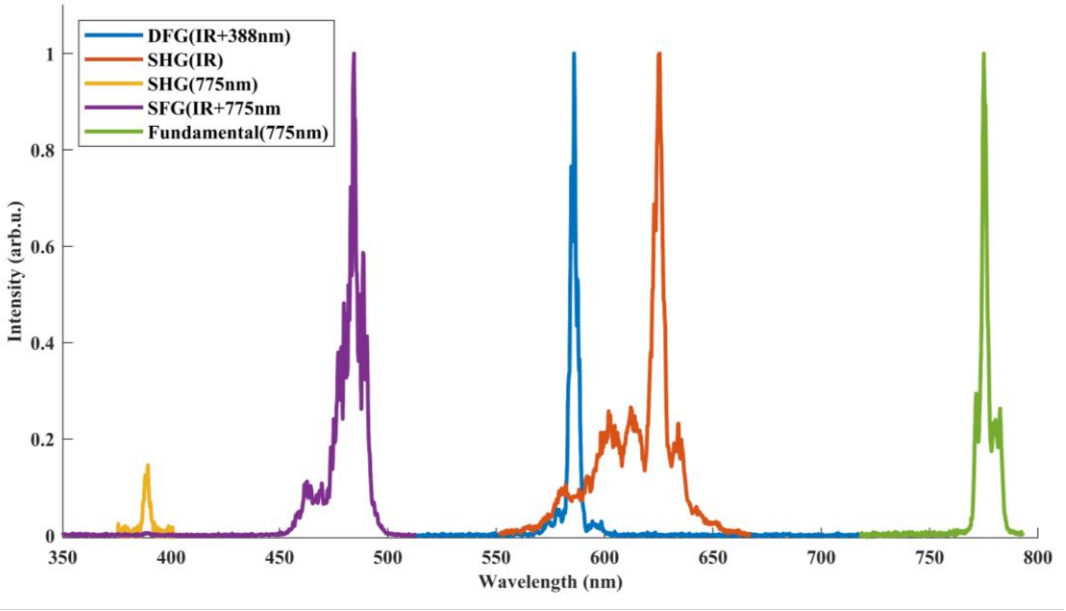

Figure 19: The spectral contents of each of the parasitic beams.

As these processes are parasitic in their diversion of energy away from the intended process of DFG between the fundamental and NIR pulse, they are ideally suppressed. A few steps can be considered to suppress these processes.

A thicker nonlinear crystal will decrease the phase matching bandwidth of these processes and stop them from diverting energy from the intended DFG process. The phase matching bandwidth will also be reduced for the DFG process, and it will be experimentally more difficult to obtain amplification. A balance should therefore be found between amplification gained by the suppression of the parasitic processes and the phase matching bandwidth of a thin crystal.

Another solution is to use a geometry for the noncollinear amplification that suppresses parasitic processes as in [41]. This is done by compensating for the walk-off resulting from the crystal birefringence. A walk-off compensating noncollinear amplification setup is designed such that the walk-off experienced by a beam (typically the pump) is in the direction of the seeding pulse wavevector.

4.4 Experimental Realization

Two visible-NIR NOPAs were set up for the tuneable generation of two different NIR pulses in the range 1-2 μm. A third setup for the generation of MIR pulses from the NIR pulses was also built

along with an autocorrelator for measurement of its duration. Final generation of MIR pulse could however not be performed due to the Clark-MXR CPA laser not functioning and no fundamental pulses could be produced. The laser power supply seems to be faulty and is in need of repair by the manufacturer.

4.5 TIME -DOMAIN PTYCHOGRAPHY

One of the first planned experiments with the MIR pulses was the measurement of the vibrational resonances in molecules and the reconstruction of these resonances using time domain ptychography. The first step in this process is to first simulate data and ensure that the reconstruction algorithm performs as expected. To generate simulated measurements for the ptychographic reconstruction, we define a complex linear susceptibility. This susceptibility emulates the vibrational transitions of a material similar to the octadecanethiol used by [30] with resonances around 3000 cm^{-1}. The different components of the simulated susceptibility with vibrational lines at 2910 cm^{-1} and 3050 cm^{-1} is shown in Figure 20.

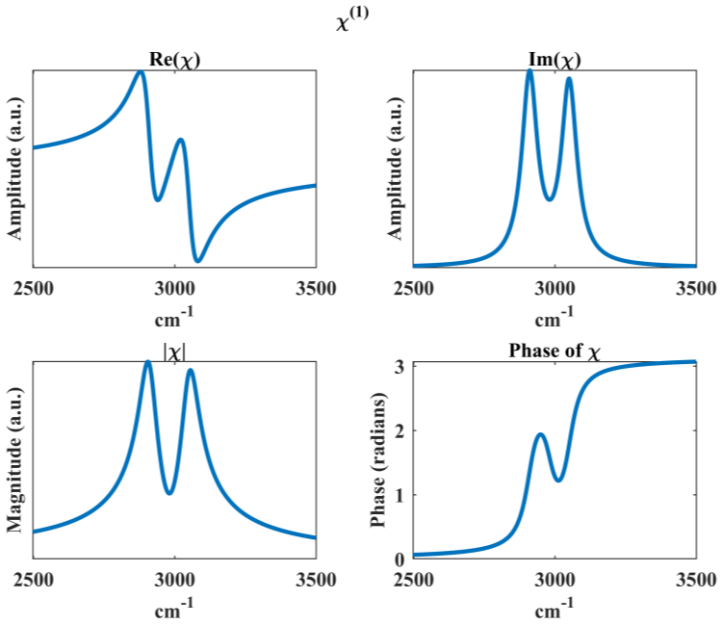

Figure 20: The different components of the complex linear susceptibility, $\chi^{(1)}$. Top left and right shows the real and imaginary parts of the susceptibility, respectively. The bottom panels show the magnitude and phase.

The susceptibility interacts with the infrared pulse, $E_{IR}(t)$, to produce the linear polarization. The susceptibility, infrared pulse, linear polarization, and probe pulse are shown in the time domain in Figure 21. The probe pulse and polarization are overlapped at 7 different delays of the probe pulse. The delays are separated by 400 fs so that consecutive probe delays overlap with a common section of the linear polarization. This helps to improve the convergence of the PIE reconstruction.

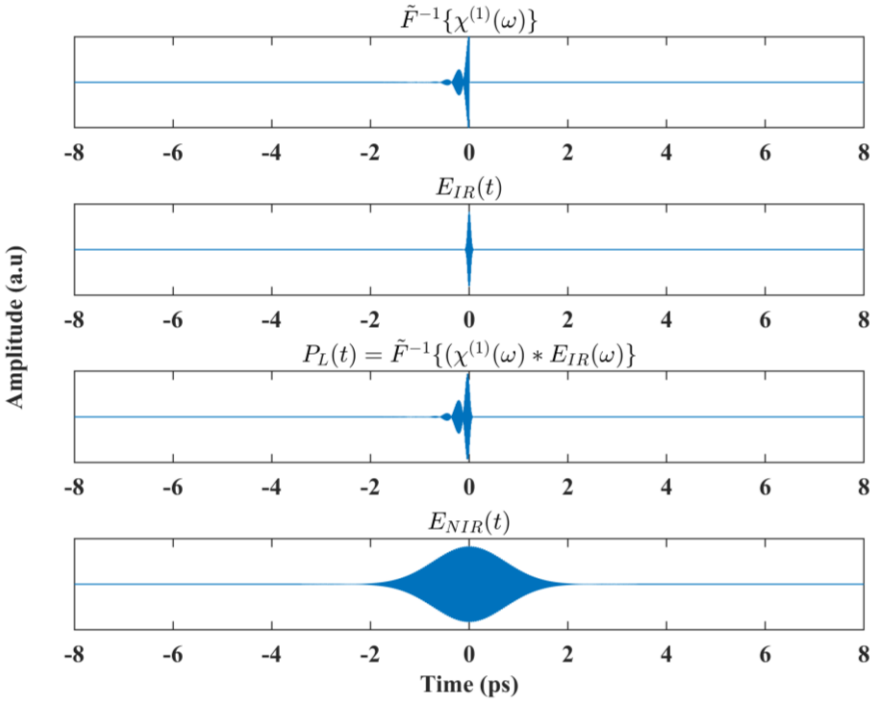

Figure 21: The different pulses in the time domain. The top graph shows the susceptibility Fourier transformed to the time domain. The second graph displays the broadband transform limited IR pulse in time with a duration of approximately 67 fs. The third graph displays the linear polarization as a result of the interaction of the susceptibility with the IR pulse. The bottom graph shows the 1.7 ps NIR probe pulse.

Spectra of each probe delay relative to the linear polarization is combined into a spectrogram in Figure 22. The top spectrogram shows the difference frequency and sum frequency generation of these pulses. In an experiment, only the sum frequency would be measured, and the bottom spectrogram shows the input sent to the PIE reconstruction algorithm. The input consists of the spectrogram along with a calibration of the wavelength axis and delay times. 67 different probe delays, separated by 200 fs, are given. Only simulated data at 7 measurements, separated by 400 fs are needed for the reconstruction of the linear polarization. This highlights one of the advantages of the HIPPY algorithm in that it does not require a large number of data sets in order to be able to reconstruct an object.

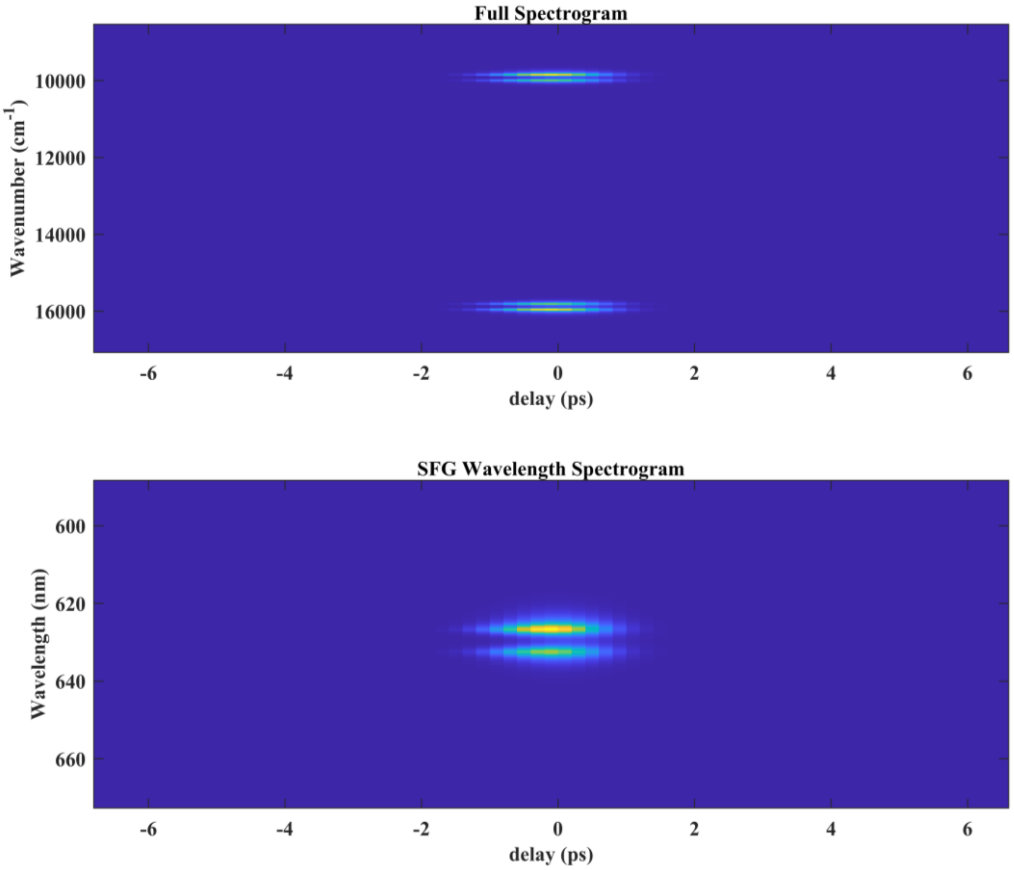

Figure 22: The spectrogram generated by the simulation is given in the top figure. Here two main bands appear for the difference and sum frequencies of the probe and linear polarization pulses. The bottom spectrogram shows the sum frequency response that simulates measured data for a SFG spectroscopy experiment, calibrated in wavelength.

The iterative engine reconstructs the object polarization pulse and the results are plotted in Figure 23. The top spectrogram is the input used in the reconstruction of the pulse. It represents the 7 spectra for different delays of the probe pulse. The lower spectrogram is the corresponding spectrogram for the reconstructed pulse at those probe delay times. Both spectrograms are plotted using logarithmic scale for better comparison of the spectral intensities. The bottom left of Figure 23 shows the reconstructed polarization amplitude in time. The overlapping probe pulse is shown for a single delay as well as the windowing function used by the PIE algorithm. The final panel in Figure 23 gives the amplitude of the reconstructed polarization along with the originally defined polarisation amplitude. The line shape and magnitude of the reconstructed polarization very closely matches that of the simulated data.

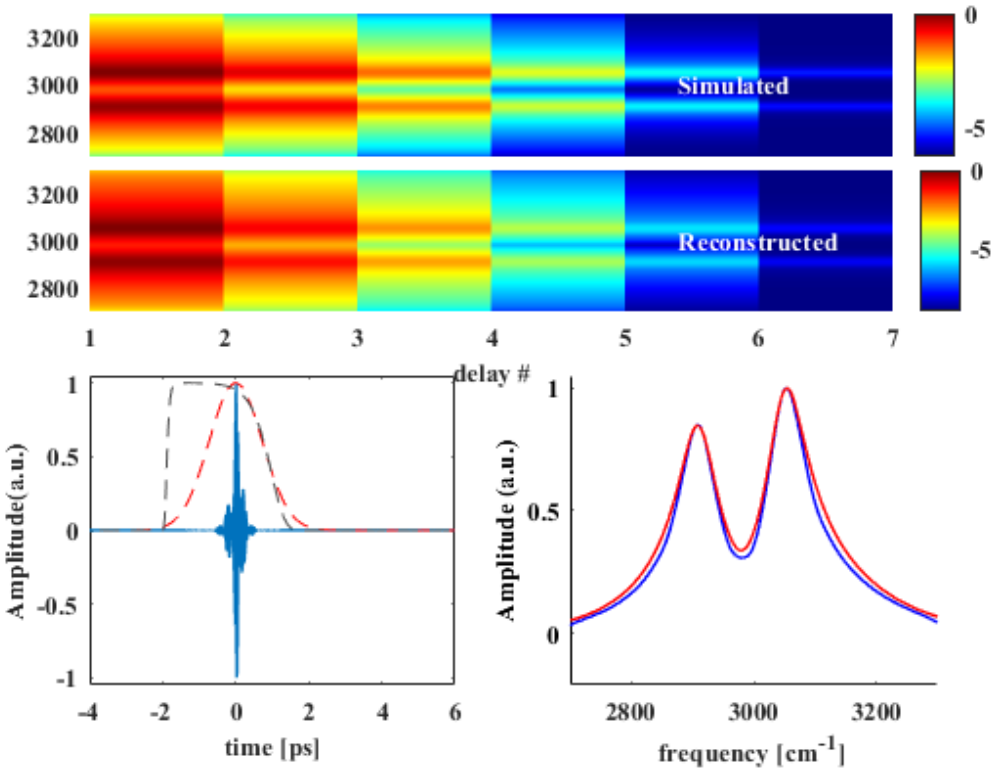

Figure 23: These figures are the results of the reconstruction of the object pulse by the PIE algorithm. The top figure compares the intensity plots for seven different delays of the probe pulse for the simulated spectra and the reconstructed spectra on logarithmic scale. Bottom left shows the reconstructed temporal object pulse in blue. The probe pulse and a noise suppressing window function is shown in red and black, respectively. Bottom right shows the reconstructed amplitude of $P_L(\omega)$ in blue along with the simulated amplitude in red.

The PIE reconstructs the linear polarization and not the susceptibility. If the mid-infrared pulse is known and well characterised, the susceptibility can be extracted. Also, if a short mid-infrared pulse with a much larger bandwidth compared to the investigated vibrational structure is used to induce the polarization, the shape of the polarization amplitude closely resembles that of the susceptibility. Temporally, this is explained because the MIR pulse is almost delta function-like compared to the time-domain susceptibility as seen in the top 2 graphs of Figure 21. In the frequency domain the modelled MIR pulse is also much broader than the simulated vibrational structure. In the frequency region of the susceptibility peaks the MIR pulse bandwidth is reasonably flat. The induced polarization amplitude then closely resembles the susceptibility amplitude in shape because of this.

5 Summary and Conclusion

This MSc project aimed to design and develop a MIR NOPA for the generation of ultrafast optical pulses at mid infrared wavelengths. These pulses would make a fine addition to the available pulses

in the Ultrafast Lab at the LRI for use in pump-probe spectroscopy experiments where molecular transition and crystal vibrations in the infrared need to be probed. This thesis proposes a setup consisting of two visible-NIR NOPAs and one MIR NOPA to this end. This configuration allows great freedom to choose the parameters of the pulses incident on the final MIR NOPA, and hence the MIR NOPA output. The proposed setup should produce MIR pulses with durations comparable to that of a NOPA pumped by the signal and idler of a Ti:Sapphire pumped OPA. A background free autocorrelator was also designed to measure the pulse duration of the generated pulses. This autocorrelator was used to measure the duration of the fundamental pulse to confirm its rated specifications as well as serve as a proof of concept for the measurement of MIR pulse durations.

The limitations of seeding a NOPA by a supercontinuum were also demonstrated. The intensity of the NIR section of the supercontinuum is too low to be useful, especially when compared to DFG that generates much higher intensities of NIR light.

Nonlinear parasitic processes were shown to be present and reduce the efficiency of the intended DFG process. These extra processes result in additional pulses at various visible wavelengths being produced. Their origins were determined by their spectra and possible methods of suppression was discussed.

Lastly, a novel use of time-domain ptychography to measure the linear susceptibility of a material was simulated, specifically using vibrational sum frequency generation. This ptychographic technique uses an intensity spectrogram of SFG which is generated by delaying a probe pulse with respect to the temporally evolving linear polarisation resulting from a MIR pulse's interaction with a material susceptibility. The spectrogram and probe pulse shape are used by the Ptychographic Iterative Engine to reconstruct the induced polarization. The simulation in this thesis involved the generation of such a spectrogram for a molecule with two absorption lines and pulses that will be available in the Ultrafast lab, after the final implementation of the MIR NOPA. The fundamental pulse was modelled as the probe, while the interaction of a chosen complex susceptibility with a feasible MIR pulse from the MIR NOPA was modelled for the linear polarisation. The reconstruction of the polarization successfully reproduced the vibrational line shapes and closely matched the amplitude of the originally simulated susceptibility. This result provides motivation for HIPPY experiments in the Ultrafast lab that will extend its capabilities. It also gives a neat example of the use of ultrafast MIR pulses.

BIBLIOGRAPHY

[1] T.H. Maiman, Nature **187**, 493 (1960).

[2] P.A. Franken, A.E. Hill, C.W. Peters, and G. Weinreich, Phys. Rev. Lett. **7**, 118 (1961).

[3] J.A. Giordmaine and R.C. Miller, Phys. Rev. Lett. **14**, 973 (1965).

[4] E. Riedle, M. Beutter, S. Lochbrunner, J. Piel, S. Schenkl, S. Spörlein, and W. Zinth, Appl. Phys. B Lasers Opt. **71**, 457 (2000).

[5] P.W. Milonni and J.H. Eberly, *Laser Physics* (John Wiley & Sons, 2010).

[6] C. Chudoba, E. Riedle, M. Pfeiffer, and T. Elsaesser, Chem. Phys. Lett. **263**, 622 (1996).

[7] U. Megerle, I. Pugliesi, C. Schriever, C.F. Sailer, and E. Riedle, Appl. Phys. B Lasers Opt. **96**, 215 (2009).

[8] A.H. Zewail, J. Phys. Chem. A **104**, 5660 (2000).

[9] N. Everall, T. Hahn, P. Matousek, A.W. Parker, and M. Towrie, Appl. Spectrosc. **55**, 1701 (2001).

[10] P. Matousek and A.W. Parker, Appl. Spectrosc. **60**, 1353 (2006).

[11] D.M. Willberg, J.J. Breen, M. Gutmann, and A.H. Zewail, J. Phys. Chem. **95**, 7136 (1991).

[12] J.W. Perry, N.F. Scherer, and A.H. Zewail, Chem. Phys. Lett. **103**, 1 (1983).

[13] J. Workman, *The Handbook of Organic Compounds, Three-Volume Set* (2000).

[14] E. Rohwer, C. Richter, N. Heming, K. Strauch, C. Litwinski, T. Nyokong, D. Schlettwein, and H. Schwoerer, ChemPhysChem **14**, 132 (2013).

[15] Z. Birech, M. Schwoerer, T. Schmeiler, J. Pflaum, and H. Schwoerer, J. Chem. Phys. **140**, 114501 (2014).

[16] E. Rohwer, I. Minda, G. Tauscher, C. Richter, H. Miura, D. Schlettwein, and H. Schwoerer, ChemPhysChem **16**, 943 (2015).

[17] I. Minda, E. Ahmed, V. Sleziona, C. Richter, M. Beu, J. Falgenhauer, H. Miura, D. Schlettwein, and H. Schwoerer, Phys. Chem. Chem. Phys. **18**, 8938 (2016).

[18] A.A. Adeniyi, P.-F.X. von Stein, G.W. Bosman, C.M. Steenkamp, T. Chiweshe, K.G. von Eschwege, and J. Conradie, J. Opt. Soc. Am. B **37**, A356 (2020).

[19] K.G. Von Eschwege, G. Bosman, J. Conradie, and H. Schwoerer, J. Phys. Chem. A **118**, 844 (2014).

[20] H. Schwoerer, K.G. von Eschwege, G. Bosman, P. Krok, and J. Conradie, ChemPhysChem **12**,

2653 (2011).

[21] S. Haidar, E. Niwa, K. Masumoto, and H. Ito, J. Phys. D. Appl. Phys. **36**, 1071 (2003).

[22] R.W. Boyd, *Nonlinear Optics*, 3rd ed. (Academic Press, Burlington, Massachusetts, 2008).

[23] J.C. Diels and W. Rudolph, *Ultrashort Laser Pulse Phenomena*, 2nd ed. (Elsevier Science & Technology, Amsterdam, 2006).

[24] C. Rullière, *Femtosecond Laser Pulses: Principles and Experiments*, 2nd ed. (Springer, New York, 2003).

[25] J.D. Jackson, *Classical Electrodynamics*, 3rd ed. (Wiley, New York, 1999).

[26] T. Brabec and F. Krausz, Phys. Rev. Lett. **78**, 3282 (1997).

[27] Y.R. Shen, *The Principles of Nonlinear Optics* (Wiley, New York, 1984).

[28] L. Valzania, T. Feurer, P. Zolliker, and E. Hack, Opt. Lett. **43**, 543 (2018).

[29] D. Spangenberg, P. Neethling, E. Rohwer, M.H. Brügmann, and T. Feurer, Phys. Rev. A - At. Mol. Opt. Phys. **91**, 021803 (2015).

[30] T. Schweizer, B.G. Nicolau, P. Cavassin, T. Feurer, N. Banerji, and J. Réhault, Opt. Lett. **45**, 6082 (2020).

[31] A.L. Mifflin, L. Velarde, J. Ho, B.T. Psciuk, C.F.A. Negre, C.J. Ebben, M.A. Upshur, Z. Lu, B.L. Strick, R.J. Thomson, V.S. Batista, H.F. Wang, and F.M. Geiger, J. Phys. Chem. A **119**, 1292 (2015).

[32] J. Piel, M. Beutter, and E. Riedle, Opt. Lett. **25**, 180 (2000).

[33] Y. V Aulin, A. Tuladhar, and E. Borguet, Opt. Lett. **43**, 4402 (2018).

[34] H. Pires, M. Baudisch, D. Sanchez, M. Hemmer, and J. Biegert, Prog. Quantum Electron. **43**, 1 (2015).

[35] J.B. Ashcom, R.R. Gattass, C.B. Schaffer, and E. Mazur, J. Opt. Soc. Am. B **23**, 2317 (2006).

[36] J. Darginavičius, G. Tamošauskas, A. Piskarskas, G. Valiulis, and A. Dubietis, Appl. Phys. B Lasers Opt. **108**, 1 (2012).

[37] U. Simon, C.E. Miller, C.C. Bradley, R.G. Hulet, R.F. Curl, and F.K. Tittel, Opt. Lett. **18**, 1062 (1993).

[38] S. Haidar, K. Nakamura, E. Niwa, K. Masumoto, and H. Ito, Appl. Opt. **38**, 1798 (1999).

[39] V. Petrov, F. Rotermund, and F. Noack, J. Opt. A Pure Appl. Opt. **3**, R1 (2001).

[40] F. Seifert, V. Petrov, and M. Woerner, Opt. Lett. **19**, 2009 (1994).

[41] J. Bromage, J. Rothhardt, S. Hädrich, C. Dorrer, C. Jocher, S. Demmler, J. Limpert, A. Tünnermann, and J.D. Zuegel, Opt. Express **19**, 16797 (2011).